QA/NA

UCRL-TR-215277

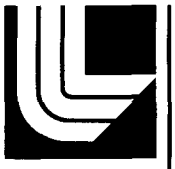

LAWRENCE
LIVERMORE
NATIONAL
LABORATORY

The Passive Film on Alloy 22

C. A. Orme

September 12, 2005

Disclaimer

This work was performed under the auspices of the U.S. Department of Energy by University of California, Lawrence Livermore National Laboratory under Contract W-7405-Eng-48.

THE PASSIVE FILM ON ALLOY 22

Christine A. Orme
Lawrence Livermore National Laboratory
L-350, P.O. Box 808
Livermore, CA 94550
orme1@llnl.gov

THIS PAGE INTENTIONALLY LEFT BLANK

1. INTRODUCTION 1
2. FORMATION OF PASSIVE FILMS ON ALLOYS 2
3. EXPERIMENTAL DETERMINATION OF THE OXIDE AS A FUNCTION OF pH AND APPLIED POTENTIAL 6
3.1 Experimental Evaluation of the Oxide that Forms under Acidic Conditions 8
3.2 Experimental Evaluation of the Oxide that Forms near Neutral Conditions 14
3.3 Experimental Evaluation of the Oxide that Forms under Basic Conditions 17
3.4 Summary of Oxides Formed as a Function of pH and Applied Potential 19
4. THE EFFECT OF AGING IN SOLUTION 19
4.1. Surface Evolution After Five Years in Multi-ionic, Concentrated Pore-water Solutions 20
4.2. Surface Evolution over 8-months in Silica Containing Basic Solutions 27
5. OXIDE GROWTH RATE 30
6. OXIDE STABILITY AS A FUNCTION OF pH AND APPLIED POTENTIAL 34
7. OXIDE FORMATION DUE TO THERMAL PROCESSING 39
7.1 Oxide Formation on Solution-Annealed Alloy 22 39
7.2 Oxide Formation in Air at Elevated Temperature 43
8. SUMMARY 52
9. REFERENCES 55
9.1 Documents Cited 55
9.2 Codes, Standards, and Regulations 58
9.3 Data, Listed by Data Tracking Number 58
APPENDIX: ANALYTICAL AND TESTING DETAILS 60
A.1. Surface Analysis Techniques 60
A.2 Electrochemical Testing 60

THIS PAGE INTENTIONALLY LEFT BLANK

1. INTRODUCTION

This report describes oxide (passive film) formation on Alloy 22 surfaces when aged in air (25-750°C) and in solutions (90-110°C) over times ranging from days to 5 years. Most zero-valent metals (and their alloys) are thermodynamically unstable on the earth's surface and in its upper crust. Most will therefore convert to oxides when exposed to a surficial or underground environment. Despite the presence of thermodynamic driving forces, metals and their alloys may persist over lengthy timescales, even under normal atmospheric oxidizing conditions. One reason for this is that as metal is converted to metal oxide, the oxide forms a film on the surface that limits diffusion of chemical components between the environment and the metal. The formation of surface oxide is integral to understanding corrosion rates and processes for many of the more "resistant" metals and alloys. This report describes the correlation between oxide composition and oxide stability for Alloy 22 under a range of relevant repository environments.

In the case in which the oxide itself is thermodynamically stable, the growth of the oxide film is a self-limiting process (i.e., as the film thickens, the diffusion across it slows, and the metal oxidizes at an ever-diminishing rate). In the case where the oxide is not thermodynamically stable, it dissolves at the oxide–solution interface as the metal oxidizes at the metal–oxide interface. The system achieves a steady state with a particular oxide thickness when the oxide dissolution and the metal oxidation rates are balanced. Once sufficient metal has transferred to solution, the solution may become saturated with respect to the oxide, which is then thermodynamically stable. The driving force for dissolution at the oxide–solution interface then ceases, and the first case is obtained.

In the case of a complex alloy such as Alloy 22 (Haynes International 1997), the development and behavior of the oxide layer is complicated by the fact that different metal components (e.g., Ni, Cr, Mo, W) form distinct oxides, each of which may be stable under somewhat different environmental conditions. For one set of conditions, the oxide layer may be dominated by one or more of these metals, for another, by a different set. Furthermore, the oxide "layer" itself may consist of sub-layers of different composition.

The purpose of this report is to characterize the oxide layer obtained from Alloy 22 over a range of environmental conditions and to demonstrate that the oxide shows passive behavior. Section 2 provides background information and theoretical predictions describing the role of pH and applied potential in oxide formation and stability. It includes a review of pertinent data on similar alloys. Section 3 presents data characterizing the oxide over a range applied potential and pH. Section 4 evaluates the oxide obtained from Alloy 22 samples aged for time periods extending from one month to over five years. Section 5 presents data showing that the oxide growth rate is logarithmic in time. Section 6 discusses the stability of the oxide as determined by short-term electrochemical tests. Section 7 describes the oxide scale that forms due to thermal processing (solution annealing and in air). Taken together, the various sections in this report present an understanding of the oxide layer obtained using a variety of methodologies, techniques, and testing conditions. An Appendix provides additional information regarding surface analysis techniques and electrochemical testing.

2. FORMATION OF PASSIVE FILMS ON ALLOYS

This section reviews the behavior of passive films on various nickel- and chromium-containing alloys. Most metals and metal alloys (with the exception of noble metals) undergo the spontaneous formation of an oxide film on the surface of the metal when exposed to oxidizing conditions such as water, air, or other oxygen containing fluids and gases (Schmuki 2002). The conversion of metal to metal-oxide consumes some of the metal and is itself a form of corrosion. Thus, the oxide film will only serve as a protective layer if the growth is a self-limiting process (i.e., the film grows to a limited thickness, creates a barrier to transport of oxygen and metal as it thickens, and then stops growing). These films, which are often less than a few nanometers thick, determine the corrosion behavior of the underlying metal or alloy (Olsson and Landolt 2003).

When a metal comes into equilibrium with a solution, some fraction of the metal atoms can become soluble solution or gas species which diffuse away from the metal surface, and some fraction can convert to a solid oxide or hydroxide that remains on the metal surface. When a voltage is applied to the metal relative to the solution, reactions that favor electron transfer are biased, and the equilibrium distribution of oxides, gasses, and solution species, are shifted. The effects of pH and potential are summarized in phase diagrams first conceptualized in *Atlas of Electrochemical Equilibria in Aqueous Solutions* (Pourbaix 1974). They are calculated from thermodynamic parameters, including energy of formation, activity of the ions in solution, pH, and potential. While equilibrium phase diagrams are useful tools, oxides formed on lab timescales may be metastable phases, and the formalism assumes that bulk oxides form. It should also be noted that Pourbaix maps (pH-potential diagrams) do not provide direct information about film structure or corrosion resistance. For this, experiments were performed to correlate oxide phases with corrosion performance.

Different metal oxides and hydroxides display different behaviors in solutions of various ionic concentrations, temperature, and pH. This variety of behaviors can be exploited by alloying the metal such that it will have components that are stable in all anticipated operating conditions. The alloying components of Alloy 22 were specifically chosen to confer passivity over a wide range of applied potential and pH values. Several models have been proposed to describe why an alloying element protects the surface. These models address various mechanisms of corrosion and can often describe the same experimental results. As a result, it is difficult to say which alloying element is responsible for a specific type of corrosion resistance behavior. Differing models place emphasis on passive film structure (Lloyd et al. 2003), percolation (Qian et al. 1990; Sieradzki and Newman 1986), charge mobility (Lin et al. 1981), and charge distribution in the film.

Based on the alloying effect, an alloy can be tailored to fit a specific set of environmental conditions by selection of constituent elements that have strengths that compensate in the areas where the other elements fail. However, because of the complex nature of passive films on alloys, it is not always clear which element or combination of elements provides the passivity in a specific region. For Ni-Cr-Mo alloys, it is believed that the molybdenum provides resistance against reducing acidic environments; chromium against oxidizing conditions; chromium and molybdenum against localized attack; and nickel, chromium, and molybdenum against stress corrosion cracking due to chloride ions (Friend 1980).

The computer program EQ3/6 was used to make thermodynamic calculations to determine the equilibrium oxide phases at two Eh and two pH points. The supporting thermodynamic database employed in these calculations was the "non-Pitzer" data file known as data0.ymp.R2 (DTN: MO0302SPATHDYN.000). Table 1 summarizes the solid phases that form when 1 g of Alloy 22 is reacted with 1 kg of 1 molal (mol/kg solvent water) NaCl at 90°C. The pH values were chosen near target experimental conditions, and the voltage values are within the passive regions. At pH 2.8, these results predict that Cr_2O_3 (eskolaite) will be the major oxide species with minor contributions from $NiWO_4$. An iron and molybdenum oxide, $Fe_2(MoO_4)_3$, should appear as the voltage is increased. Near neutral pH, nickel oxides are expected. Cr_2O_3 is undersaturated at pH 7.5, and chromium is predominantly in the spinel phase $NiCr_2O_4$. At the higher potential value, there are no thermodynamically stable chromium oxides that are expected to be in equilibrium with the solution.

Table 1. Results From EQ3/6 Showing the Equilibrium Oxide Phases that Form when 1 g of Alloy 22 is Reacted with 1 kg of 1 molal NaCl Solution at 90°C

pH (NBS scale)	Potential (V)	V vs. Ag/AgCl	Mineral	Formula	Moles
2.8	0.22	0	Eskolaite	Cr_2O_3	2.10×10^{-3}
				$NiWO_4$	1.63×10^{-4}
2.8	0.57	0.35	Eskolaite	Cr_2O_3	2.10×10^{-3}
				$Fe_2(MoO_4)_3$	2.65×10^{-4}
				$NiWO_4$	1.63×10^{-4}
7.5	-0.09	-0.31	Bunsenite	NiO	7.42×10^{-3}
				$NiCr_2O_4$	1.69×10^{-3}
				$CoCr_2O_4$	4.24×10^{-4}
			Trevorite	$NiFe_2O_4$	2.69×10^{-4}
				$NiWO_4$	1.53×10^{-4}
7.5	0.49	0.27	Bunsenite	NiO	9.11×10^{-3}
			Trevorite	$NiFe_2O_4$	2.69×10^{-4}
				$NiWO_4$	1.52×10^{-4}
				Spinel-Co	1.41×10^{-4}
				MnO_2 (gamma)	9.10×10^{-5}

Source: DTN: LL040502712342.006.

These calculations give the equilibrium oxide phases with a relatively high concentration of metal in the solution (approximately 0.01 mol/L). In the experiments discussed, the metal solution concentrations are several orders of magnitude smaller (approximately 10^{-5} mol/L) due to the slow dissolution rate of Alloy 22 and the large solution volumes used. It is therefore expected that the measured oxides are likely to be undersaturated with respect to the solution phase and represent kinetically stable phases rather than thermodynamically stable phases. Nevertheless, as will be seen in upcoming sections, the kinetically formed film has oxide phases that are consistent with those expected to evolve in equilibrium.

Literature Survey of Oxide Formation–This section reviews the properties of the passive oxide films of several nickel- and chromium-containing industrial analogs of Alloy 22. In most

cases, systems exposed to similar environments as the present study are highlighted (i.e., aqueous NaCl solutions in various pH buffers and at various potentials).

Nickel-Based Alloys–There are a considerable number of commercial Ni-Cr and Ni-Cr-Fe alloys (Piron et al. 1969). For example, Inconel 600 is a well-known Ni-Cr-Fe alloy. Inconel 600 is used in place of Ni 200 when a higher strength material is required or moderately sulfurizing conditions are present. Additionally, Inconel 600 is used extensively in the steam generators of pressurized water reactors in the nuclear industry.

Ni-Cr-Mo alloys exhibit excellent corrosion resistance in both oxidizing and reducing environments and are considered the most corrosion resistant of the nickel-based super alloys. Consequently, many of these alloys are used in industrial applications. Some well-known industrially applied alloys include Hastelloy C-4, Hastelloy X, Hastelloy C-276, and Inconel 625. An excellent review of the corrosion resistance properties of each is detailed in the literature (Friend 1980).

The addition of molybdenum to nickel-based alloys has been shown to decrease corrosion rates with increasing molybdenum content. Several plausible explanations for the mechanisms responsible for increased corrosion resistance with increased molybdenum content have been developed. Among these, it has been proposed that a primary function of molybdenum is to retard the propagation of localized corrosion once the passive film breakdown has occurred. It has been postulated that molybdenum preferentially locates at local defects on the surface, which otherwise would act as dissolution sites (Lloyd et al. 2003).

Chemical Composition–XPS measurements have been utilized to study the chemical composition of the passive films of several Ni-Cr alloys after 24-hour immersion in 0.1 mol/L NaCl solution (Lim and Atrens 1992). XPS analyses showed that, for each Ni-Cr alloy, the oxide film contained only Cr_2O_3. Electrochemical techniques were used for the determination of the relative corrosion rate of the alloys. The results showed that Ni-Cr10 and Ni-Cr20 alloys showed a slightly higher corrosion rate than Ni-Cr40.

Jabs et al. (1997), using XPS, have studied the chemical compositions of passive films of Ni-Cr alloys in both basic (1 mol/L NaOH) and acidic (0.5 mol/L H_2SO_4) environments. In NaOH solutions, the thickness and composition of the passive layer as a function of passivation potential was characterized. The passive film of Ni-Cr20 in both 0.5 mol/L H_2SO_4 and 1 mol/L NaOH solutions exhibited a bilayer structure with an oxide interfacial layer and an overlying hydroxide layer above it. In 1 mol/L NaOH, nickel is enriched at the metal surface and forms the hydroxide layer, especially at positive potentials and for long passivation times. The oxide layer consisted mainly of Cr_2O_3. NiO was also present in the passive film but entered only in the transpassive potential region (> 600 mV versus standard hydrogen electrode). The thickness of the passive film increased linearly with potential (from 1 nm at –500 mV versus standard hydrogen electrode to 5 nm at 600 mV versus standard hydrogen electrode). In acidic solutions (0.5 mol/L H_2SO_4), the oxide and the hydroxide part of the passive film contained only Cr(III) ions with minor evidence of Ni(II) and Cr(VI) in the transpassive range. The passive film thickness for acidic solutions was a linear function of the potential. The thickness of the passive film increased linearly with potential from 0.5 nm at −500 mV versus standard hydrogen electrode to 3 nm at 600 mV versus standard hydrogen electrode. The fact that the passive oxide

film is thicker in basic solutions has also been observed in stainless steel alloys (Schmutz and Landolt 1999).

Marcus and Grimal (1992) used XPS to characterize the passive film of Ni-Cr-Fe alloys that closely resemble Inconel 600 in dilute acidic solution (0.05 mol/L H_2SO_4). XPS analyses of passive layers formed on Ni-Cr21-Fe8 at 300 mV versus standard hydrogen electrode and 600 mV versus standard hydrogen electrode demonstrated the existence of a bilayer structure. The inner oxide layer consisted of approximately 96% Cr_2O_3 and 4% Fe_2O_3. There was no detectable Ni(II). The outer hydroxide layer was approximately 100% $Cr(OH)_3$. At 300 mV versus standard hydrogen electrode, the thickness of the passive film was 1.1 nm, and the thickness of the inner oxide layer was 0.65 nm. At 600 mV versus standard hydrogen electrode, the film was thicker (the thickness of the inner oxide layer was 0.9 nm).

The passive film for Hastelloy Alloy C-276 and Alloy 22 in 1 mol/L NaCl + 0.1 mol/L H_2SO_4 has been characterized using XPS for chemical composition and time of flight secondary ion mass spectroscopy (TOF-SIMS) for passive film thickness (Lloyd et al. 2003). The passive film on Alloy 22 exhibits a bilayer structure. TOF-SIMS analyses show a layered oxide structure consisting of a Mo/Cr oxide-rich outer layer and Cr/Ni oxide-rich inner layer. Although the bilayer persists at potentials ranging from 200 mV to 700 mV versus Ag/AgCl, the concentration percentages of the oxides in the two layers were a function of potential. In general, the overall chromium content increased steadily, and the nickel content decreased with increasing potential. The increase in chromium content was predominantly within the inner regions of the film. Based on XPS results, the oxidation states in the passive film were NiO, Cr_2O_3, and MoO_3. It is important to note that there was no evidence of Cr(VI) within the oxide film, indicating that oxidative dissolution leads to the release of all Cr(VI) species formed to the solution. By contrast, Mo(VI) was retained as the dominant species in the oxide at higher potentials.

Oxide thicknesses increased linearly with potential (Lloyd et al. 2003). The thicknesses, determined by TOF-SIMS analyses, were measured to be 2.0 nm at 200 mV, 2.3 nm at 500 mV, and 2.8 nm at 700 mV versus Ag/AgCl. In general, the oxide thicknesses on Alloy 22 are similar to those mentioned above for Ni-Cr alloys (Jabs et al. 1997).

The passive film of Alloy 276 does not show as clear a bilayer structure as Alloy 22, but it does contain the same constituents. The chromium content of the oxide was lower on C-276 than Alloy 22 and only increased significantly after the potential was raised into the transpassive region (>700 mV versus Ag/AgCl). The overall molybdenum content of the oxide on C-276 was significantly higher than on Alloy 22. Lloyd et al. (2003) commented that the inability of C-276 to retain chromium within a barrier layer at the alloy–oxide interface may explain the greater sensitivity of this alloy to localized corrosion at increasing temperature.

Film Stability–Hodge and Wilde (1970), using anodic polarization techniques in 0.5 mol/L H_2SO_4 + 1 mol/L NaCl at 25°C, found that Ni-Cr alloys containing more than 10% chromium develop passivity and are resistant to dilute sulfuric acid solutions containing certain amounts of chloride. A similar effect of the addition of chromium to nickel was shown by Piron et al. with a potentiostatic anodic polarization study of Ni 200 and Inconel 600 in 0.5 mol/L H_2SO_4 solutions at 24°C, to which was added sodium chloride in various amounts from 0 to 3.5 wt % (Piron et al. 1969). A quantitative measure of the effect of chloride ions on the passivity of those two

materials in 0.5 mol/L H_2SO_4 was achieved by maintaining the potential of each electrode within the passive region (+600 mV versus standard hydrogen electrode in the case of Inconel and +500 mV versus standard hydrogen electrode in the case of nickel). Subsequently, the concentration of chloride ions was increased by the addition of increments of a concentrated sodium chloride solution. At each concentration, the steady state passive current density was measured. The results showed that, for each material, the breakdown of passivity occurred at a critical NaCl concentration (Friend 1980).

The stability of the passive films of several Ni-Cr-Mo alloys has been discussed in detail (Friend 1980). In summary, Alloys C, C-276, C-4, and Inconel alloy 625 have been tested for corrosion resistance in titrated acidic solutions, including HCl, H_2SO_4, HNO_3, HF, and HPO_3. The alloys with higher molybdenum content usually show the best resistance to reducing environments such as H_2SO_4 and HCl and pitting attacks from chloride-containing solutions, while the alloys with higher chromium content usually have the best resistance to strongly oxidizing solutions such as nitric acid (Friend 1980).

3. EXPERIMENTAL DETERMINATION OF THE OXIDE AS A FUNCTION OF pH AND APPLIED POTENTIAL

To determine the oxide phases responsible for passive behavior, oxide films were grown on Alloy 22 at several pH and applied potential values. Specimens were tested in complex multi-ionic solutions that were based on concentrated repository ground waters (see Orme 2003a, Orme 2003b, and Orme 2004 for solution compositions). These solutions are referred to as simulated acidic water, (SAW), simulated concentrated water (SCW), and basic saturated water (BSW). In addition, simplified, buffered solutions were used to allow a better comparison with theoretical models and literature. This work focuses on three pH values with nominal values 3, 8, and 11; these solutions are designated "pH3," "pH8," and "pH11," respectively (but only electrochemical tests were conducted at pH 11). The pH values cited are approximate.

The voltages were chosen by examining the anodic polarization curves. These current-voltage plots are shown in Figure 1 for the buffered 1-mol/L NaCl solution and in Figure 2 for the multi-ionic solutions. It should be noted that the curves at similar pH levels are almost identical for the simplified and multi-ionic solutions. The observation that the current-voltage curves are a function of pH, independent of the ionic species found in repository solutions, removes one level of complexity from the problem of determining the oxide film in all relevant repository conditions.

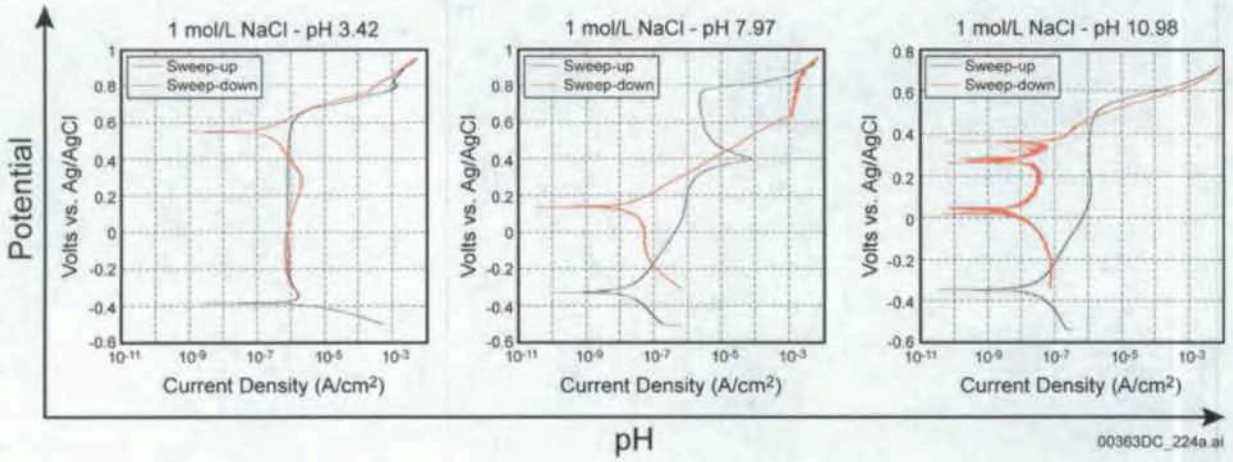

Source: DTN: LL040505512251.101.

NOTE: Curves are shown for pH values of 3.42 (DEA 569), 7.97 (DEA 568), and 10.98 (DEA 1102). The forward (anodic) voltage scan is shown in black, and the reverse cathodic voltage scan is shown in red.

Figure 1. Potentiodynamic Scans of Alloy 22 in Buffered 1-mol/L NaCl Solutions

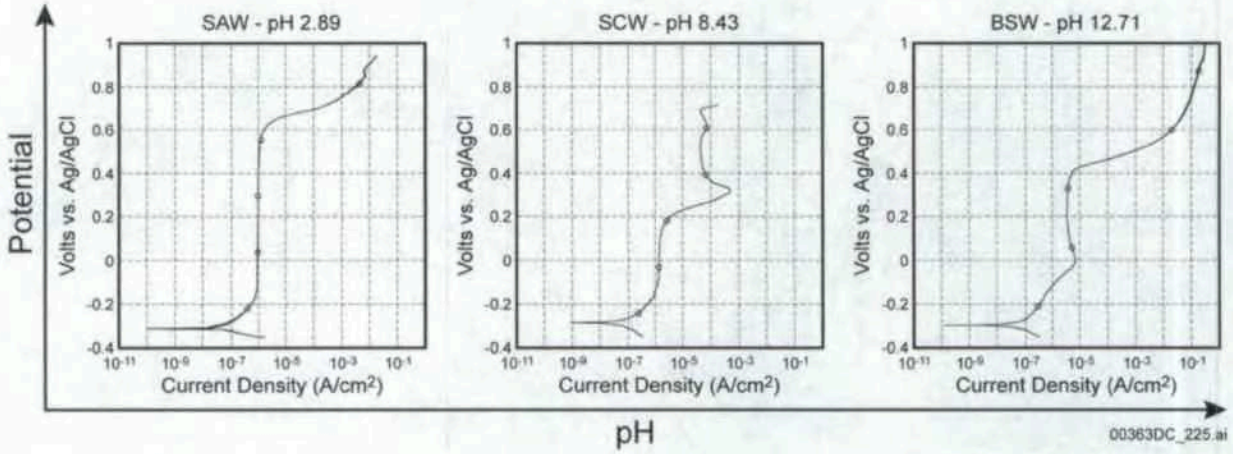

Source: DTNs: LL040505512251.101.

NOTE: Curves are shown for pH values of 2.89 (DEA 492), 8.43 (DEA 1246), and 12.71 (DEA 461). The electrochemical response is almost identical to the simpler 1-mol/L NaCl solutions at similar pH values.

Figure 2. Potentiodynamic Scans of Alloy 22 in Simulated Acidified Water, Simulated Concentrated Water, and Basic Saturated Water Solutions

To characterize the oxide, films were grown potentiostatically at several voltages between the open circuit potential and the onset of transpassive dissolution. Figures 1 and 2 are organized according to increasing pH to suggest that changes in the current response may indicate a phase transition in the oxide film. As the voltage is varied, phase boundaries are traversed, and different oxide phases become stable. These transitions will affect the current response of the system. Phase changes usually involve dissolution and the flow of metal or oxygen ions (i.e.,

when a phase transition occurs, current flows). Constant current plateaus, such as seen between −300 mV and 600 mV in the pH 3 solution, suggest that this entire region has a similar oxide composition. In contrast, in solutions near pH 8, the two regions above and below the anodic peak at approximately 400 mV are likely different oxides. While this is not a rigorous analogy, these observations suggested regions in pH-potential space and these were chosen for more detailed investigations. Table 2 contains a summary of the samples, test conditions, and analysis methods discussed in this section. The three pH regions will be discussed in turn.

Table 2. Summary of Oxide Growth Conditions and Analysis Shown in this Section

Metal Alloy	Solution	pH	Sample ID	Voltage versus Ag/AgCl (mV)	Temperature (°C)	Analysis
Alloy 22	pH3	2.72	DEA 565	200	90	XPS, AES
Alloy 22	pH3	2.68	DEA 562	200	90	TEM, AFM
Alloy 22	pH3	2.87	DEA 567	500	90	TEM
Alloy 22	pH3	2.70	DEA 566	500	90	XPS, AES, AFM
Alloy 22	SAW	2.98	DEA 495	400	90	XPS
Alloy 22 Weld	pH3	3.38	JE 3022	200	90	XPS
Alloy 22 Weld	pH3	3.39	JE 3025	400	90	XPS
Alloy 22	pH8	8.12	DEA 543	200	90	TEM
Alloy 22	pH8	8.11	DEA 539	200	90	XPS, AES
Alloy 22	pH8	7.56	DEA 557	400	90	TEM
Alloy 22	pH8	8.03	DEA 518	200	90	AFM
Alloy 22	pH8	8.07	DEA 532	400	90	AFM
Alloy 22	pH8	7.56	DEA 556	400	90	XPS, AES
Alloy 22	pH8	8.03	DEA 520	650	90	TEM
Alloy 22	pH8	7.66	DEA 559	650	90	XPS, AES, AFM
Alloy 22	BSW	12.48	DEA 465	250	90	XPS
Alloy 22	BSW	12.76	DEA 496	250	90	TEM

Source: DTNs: LL040206712251.074, LL040206412251.071, LL040207512251.076, LL040207612251.077, LL040206612251.073, LL040308412251.081, LL040206512251.072, and LL040500512251.088.

NOTE: The pH value labels in the solution column are used as solution designations, representing the approximate solution pH value.

3.1 Experimental Evaluation of the Oxide that Forms under Acidic Conditions

Alloy 22 specimens were tested in solutions near pH 3. From the cyclic polarization curve in Figure 1, it can be seen that the curve has classic passive behavior with a broad, approximately 1 V flat plateau region where the current is independent of the applied potential. Two potentials at either end of the passive plateau were chosen to potentiostatically grow an oxide film. The oxides were then characterized using AFM, TEM, XPS, and AES depth profiling. The oxide films formed in two acidic solutions: multi-ionic and NaCl, which are shown to be very similar.

Oxide Formed in 1 mol/L NaCl Buffered near pH 3–A 1-mol/L NaCl solution buffered near pH 3 using phthalate was used to mimic SAW under simplified (and buffered) solution conditions. The solution pH stayed constant within 0.1 pH units during the course of any given

experiment but varied more widely between experiments. Experiments with pH values 3 ±0.4 have similar behavior and are grouped together in this analysis.

The AFM images are topographic maps of the surface morphology. The surface morphologies for films grown at 500 mV and 200 mV versus Ag/AgCl are shown in Figure 3a (top) and 3b (bottom), respectively. The images show a smooth surface with a filamentary deposit. The filamentary surface morphology has been attributed to the phthalate buffering agent because samples exposed to SAW (also near pH 3) do not show these deposits. The surface morphology after oxide growth seen in the AFM images of Figure 3 is similar to the surface morphology of the sample before the oxide was grown (image not shown), indicating that the oxide film is smooth and conformal to the metal surface.

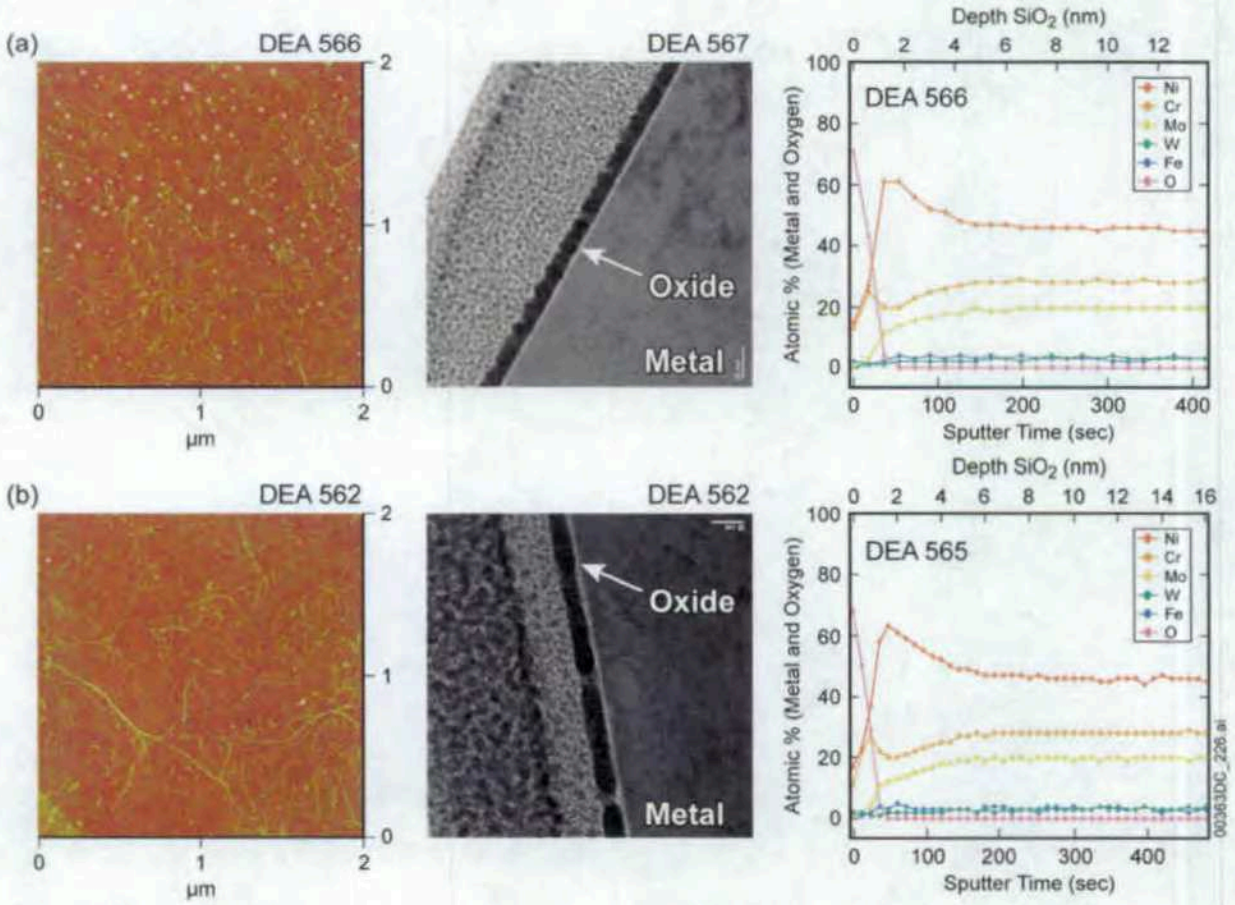

Source: DTNs: LL040206412251.071, LL040206412251.071, and LL040206512251.072.

NOTE: All voltages are versus a saturated Ag/AgCl reference electrode. The first column shows AFM images of the surface morphology (DTN: LL040206412251.071). The images are 2 μm by 2 μm and have a RMS surface roughness less than 1 nm. The second column shows a cross-sectional TEM image (DTN: LL040206412251.071). The metal is on the right-hand side. The third column is AES depth profiling showing atomic composition across the oxide and into the metal (DTN: LL040206512251.072).

Figure 3. Surface Morphology (AFM), Cross-Sectional TEM Images, and Chemical Compositions of Oxides Formed at (a) 500 mV and (b) 200 mV in 1-mol/L NaCl Solution Buffered at pH 2.7

Cross-sectional TEM images show the morphology of the oxide in a cross-sectional view and allow a direct measure of its thickness. The pluck-out samples are approximately 3 μm long, and the oxide was imaged over the full length. Figure 3 shows representative sections at 65,000x magnification. At both voltages within the passive region, a thin conformal layer can be seen at the metal surface. At the lower potential (200 mV versus Ag/AgCl), the oxide is 4.0 ±0.5 nm and is less uniform in thickness than the 2.4 ±0.3 nm film formed at the higher voltage (500 mV versus Ag/AgCl) (DTN: LL040500912251.092).

EELS images (Figure 4) show a definitive chromium and oxygen signal in the oxide region. The elemental maps are inconclusive regarding the presence of nickel in the oxide layer because the high concentration of nickel in the base metal makes the nickel difficult to see. In the chromium map, Figure 4a, there is a darker line at the metal–oxide interface indicating that this area has less chromium. This is consistent with nickel enrichment at the metal surface.

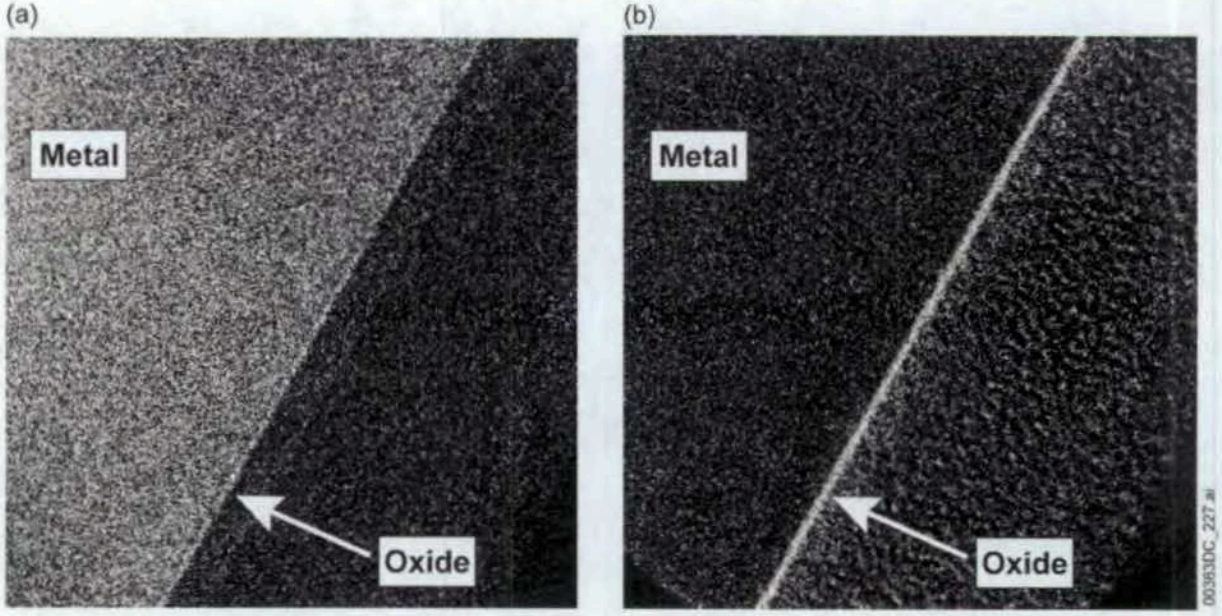

Source: DTN: LL040500512251.088.

NOTE: The maps indicate a chromium oxide barrier layer.

Figure 4. Electron Energy-Loss Spectroscopy Showing Elemental Maps of (a) Chromium and (b) Oxygen for Sample DEA567

XPS can help determine the oxidation state of the elements. In Figure 5, spectra for nickel, chromium, molybdenum, tungsten, iron, and oxygen are shown. The carbon peak is referenced to 284.8 eV. Because the oxide is relatively thin, the underlying metallic component (indicated on the figure as the metallic peak) is apparent for all Alloy 22 species. Because Alloy 22 base metal and Alloy 22 weld specimens have very similar electrochemical responses, XPS spectra, and oxide thicknesses, these samples have been grouped together to determine trends. Table 3 summarizes the speciation of the chromium and molybdenum spectra. As can be seen from Table 3, both the molybdenum and chromium spectra indicate more metallic component at lower potentials. This would typically be associated with a thinner oxide layer (which allows the electrons initiating from the metal to escape), but from the TEM cross-sectional images it is

known that the oxide is thicker on average at the lower potentials. It may be that the oxide is less dense or that the oxide is less uniform at the lower potential. At the higher applied voltage levels, the NiO peak increases relative to the metallic nickel peak and the chromium speciation shifts to a higher percentage of chromium in the 3+ state (as in Cr_2O_3).

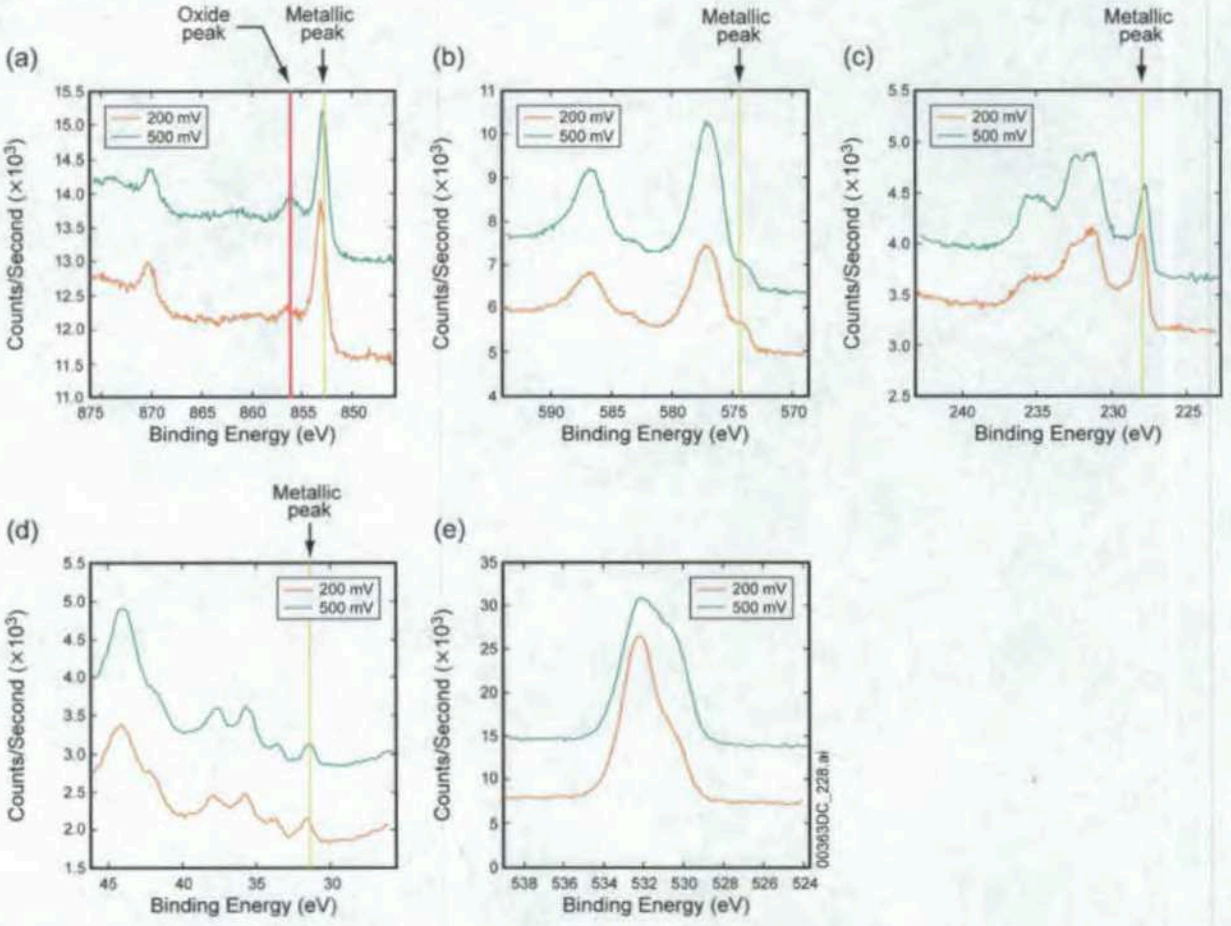

Source: DTN: LL040206712251.074; see also LLNL 2003a.

NOTE: The elemental regions are: (a) nickel, (b) chromium, (c) molybdenum, (d) tungsten, and (e) oxygen.

Figure 5. XPS Spectra of Samples Held at 200 mV (DEA565) and 500 mV (DEA566)

Table 3. Relative Speciation of Oxides, as Determined by Fitting the High-Resolution Spectra

Sample ID	Potential (mV vs. Ag/AgCl)	Auger Sputter Time (s)	Chromium (%)				Molybdenum (%)			
			Cr metal	CrO_2	Cr_2O_3, $Cr(OH)_3$, CrOOH	CrO_3	Mo Metal	MoO_2	Mo_2O_3 Hydroxide	MoO_3, Molybdate
DEA565	200	30	9.9	24.1	51.6	14.4	28.5	20	29	22.5
JE3022	200	27	8.8	18.4	54.4	18.4	33.8	16.8	17.2	32.2
JE3025	400	30	5	13	62.4	19.6	21.3	10	32.3	36.5
DEA566	500	27	5.7	17.2	60.8	16.2	22.7	11.9	32.7	32.8

Source: LLNL 2003a.

NOTE: The peaks have a large degree of overlap, and the fits may not be unique. The samples DEA565 and DEA566 are Alloy 22 base metal specimens, whereas JE3022 and JE3025 are weld specimens. The second column describes the test conditions.

Oxide Formed in Multi-ionic SAW Solution with pH 2.8–The oxide films that form in SAW solution are very similar to those formed in 1 mol/L NaCl buffered at pH 2.8 using phthalate. Figure 6a shows a cross-sectional view of an oxide formed by 16 hours of holding in SAW at a potential 200 mV versus Ag/AgCl. Figure 6b shows the XPS sputter profile. The TEM image shows a conformal oxide that measures 2.9 ±0.3 nm thick (DTN: LL040500912251.092). The XPS depth profile across the oxide reveals that oxide is almost entirely chromium oxide.

The XPS sputtering profile shows the total atomic percent of nickel, chromium, molybdenum, tungsten, and oxygen. (Iron is not shown because the concentrations are low and the peaks interfere with nickel Auger lines.) The electron escape depths for the metallic elements are approximately 3 nm, which are comparable to the oxide thicknesses. For this reason, the surface oxide spectra also show a metallic component. To account for the metal contribution in the oxide spectra, metal peak fits were performed within the base metal to obtain the positions and line shapes of the metallic components. Spectra within the oxide region were then fit with a combination of metallic and oxide peaks.

Only the chromium spectra showed distinctive oxide peaks. This allowed the chromium oxide contribution to be separated from the metallic contribution in the atomic percent calculations. Both the total chromium and the chromium oxide are shown in Figure 6b.

The oxygen signal is partially from the oxide and partially from surface contamination. To separate these contributions, the oxygen spectra were fit with two peaks at 530 and 531 eV. The peak at 530 eV is consistent with Cr_2O_3. The oxide oxygen fraction is also shown plotted in the depth profile.

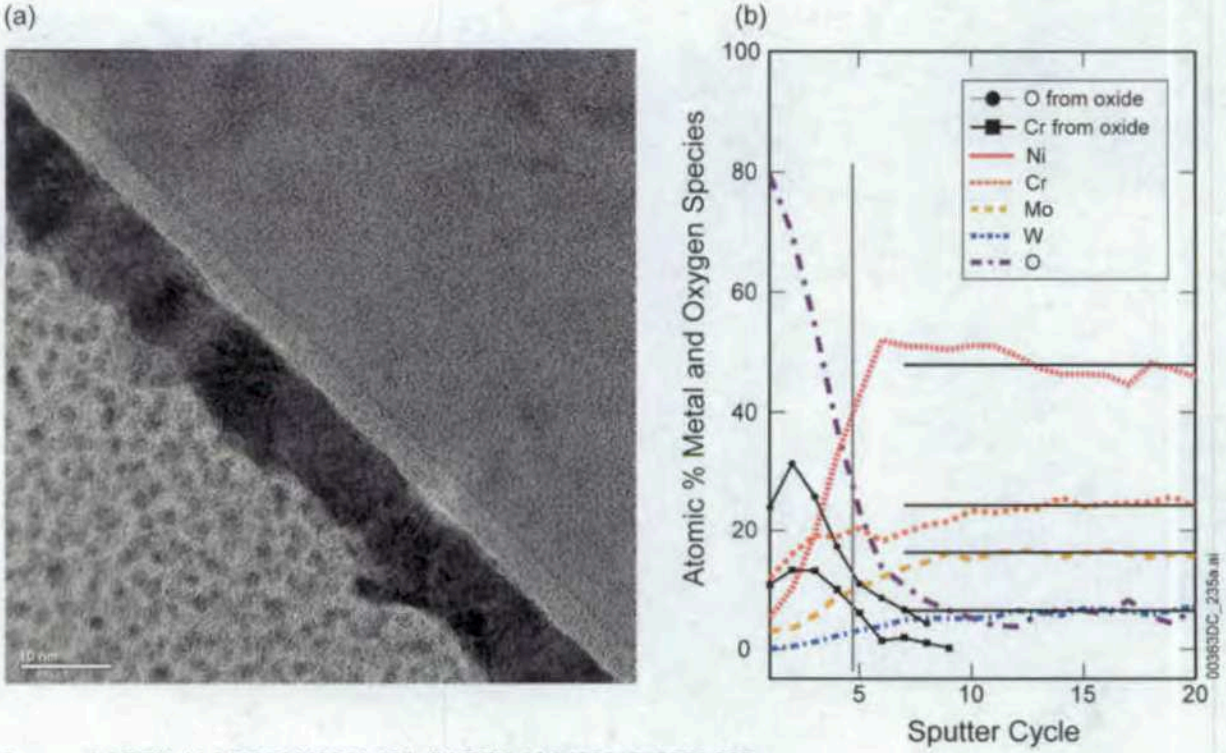

Source: (a) DTN: LL040308412251.081; (b) DTN: LL040501212251.095.

NOTE: In the depth profile, a vertical line marks the approximate location of the metal–oxide interface as determined from the half maximum value for the chromium oxide concentration. Horizontal lines mark the average values of the nickel, chromium, molybdenum, and tungsten atomic % averaged over sputtering cycles 10-36 (data were obtained for a longer duration than is presented in this graph).

Figure 6. (a) TEM of Sample DEA495 and (b) XPS Depth Profiling of Sample DEA495, Showing the Oxide Film that Forms in the Passive Region in Acidic Solutions

The nickel spectra are almost entirely metallic. Only one spectrum (at cycle 3) close to the metal–oxide boundary shows a slight broadening that may indicate a thin nickel oxide. This was observed for only one cycle, and because the signal to noise is low in this region, the data are inconclusive. The metallic nickel at the metal–oxide interface shows a slight increase in concentration over its average value deeper in the bulk. In the metal–oxide interface region, the other metals have not yet reached their average bulk values, whereas nickel has overshot its average bulk concentration. This nickel enhancement has been observed on several other systems and is associated with passivity.

In summary, the oxide film that forms in the passive region in SAW solution is a conformal, 2.9-nm-thick chromium oxide film consistent with chromium in the Cr(III) oxidation state. In the literature, it is found that the chromium oxide is hydrated at the oxide–solution interface and less hydrated at the oxide–metal interface; this is often referred to as a bilayer (Marcus and Grimal 1992). The signal-to-noise levels of these data were not high enough to fit the hydration peak with confidence. With the signal-to-noise levels of these data, no nickel, molybdenum, or tungsten oxides could be identified in the oxide layer. There is an enhancement of nickel metal at the interface between the oxide and the metal substrate.

The oxide films of unpolarized Alloy 22 substrates aged for five years in SAW at 90°C are discussed in section 4.1. The oxide composition could not be determined due to flaws in the experimental design, however the oxide did not thicken substantially with time.

3.2 Experimental Evaluation of the Oxide that Forms near Neutral Conditions

Oxide Formed in 1-mol/L NaCl Solution Buffered at pH 7.5–The surface oxide that forms in near neutral solution has two very distinct regions: one associated with a thin oxide similar to other passive films and another associated with a thick porous oxide. These two regions are suggested from the cyclic polarization curve in Figure 1, which shows two constant current plateaus separated by an anodic peak at 400 mV. The first plateau, between 0 and 300 mV is associated with passive film formation. The second plateau, between 500 and 800 mV suggests that another stable oxide phase forms. The anodic peak is indicative of the formation of a second stable oxide phase. The morphology and elemental compositions of the oxide films formed at increasing voltage are summarized in Figure 7. While the cyclic polarization showed two current regions, all potentiostatically held samples had current densities between 50 and 1,100 nA/cm^2 after 16 to 20 hours (DTNs: LL040206612251.073 and LL040207512251.076 for raw data files, or LL040500712251.090 for summary table). The final currents were independent of voltage until the transpassive region near 750 mV.

Figure 7 shows the transition in oxide as the applied potential is increased from the passive region at the bottom of Figure 7c to a voltage near transpassive dissolution shown in Figure 7a. Comparison with Figure 1 shows that these correspond to the two plateaus observed in the cyclic polarization curve.

In the passive region, a thin, smooth oxide is observed. From the AFM images, the surface roughness is approximately the same (less than 1 nm for the 2 μm by 2 μm area) before and after oxide growth. The Auger elemental depth profile in the third column shows that oxygen, nickel, and chromium have the highest concentrations in the oxide region. AES does not distinguish between elements in the metallic and oxide states, and most of the nickel signal is from the underlying metal substrate. Some of the chromium signal is also coming from the underlying metal, but the fact that the concentration peaks in the oxide demonstrates that there is chromium in the oxide region. There is a dip in the chromium concentration and a peak in the nickel signal at approximately the same depth. This is consistent with nickel enrichment in the metal.

Above approximately 300 to 350 mV, a thick, porous oxide forms, changing the morphology and surface roughness dramatically. From the AFM, images it can be seen that the oxide has a tighter pore structure at 650 mV than at 400 mV. The TEM images in the second column show two distinct layers in the oxide, with a compact thin layer (about 4 nm thick) close to the oxide and the porous (30- to 40-nm-thick) structure farther away. At 400 mV, the porous structure is irregular and open. The higher voltage has a finer pore size and a more uniform thickness. The distinction between the porous layer and the compact oxide is more apparent, and there appear to be voids that segregate at the compact, porous interface.

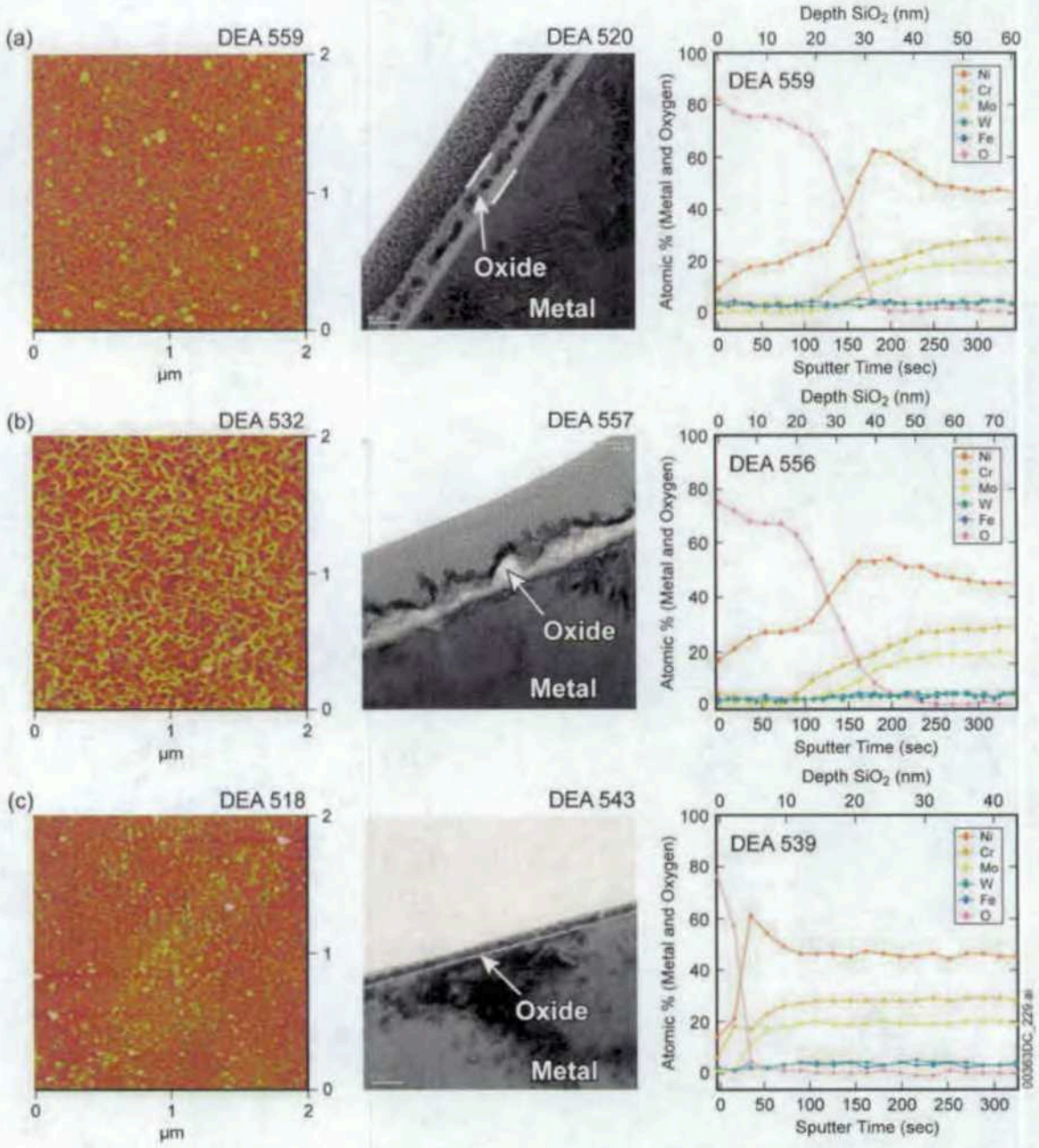

Source: DTNs: LL040206412251.071, LL040500512251.088, and LL040206512251.072.

NOTE: All voltages are versus a saturated Ag/AgCl reference electrode. The first column shows AFM images of the surface morphology (DTN: LL040206412251.071); The images are 2 μm by 2 μm. The second column shows a cross-sectional TEM image (DTN: LL040500512251.088). The metal is on the bottom half of the image. In the third column, AES depth profiling gives atomic composition across the oxide and into the metal (DTN: LL040206512251.072).

Figure 7. Surface Morphology and Cross-Sectional TEM Views of Oxides Formed at (a) 650 mV, (b) 400 mV, and (c) 200 mV in 1-mol/L NaCl Solution Buffered at pH 7.5

Figure 8 shows the XPS spectra for the Cr2p, Mo3d, and Ni2p energy intervals. The film formed at 200 mV (in the passive region) demonstrates that the oxide is predominantly chromium oxide (consistent with Cr_2O_3), with some molybdenum and nickel oxide. The surfaces of the two porous oxides are predominantly nickel oxide.

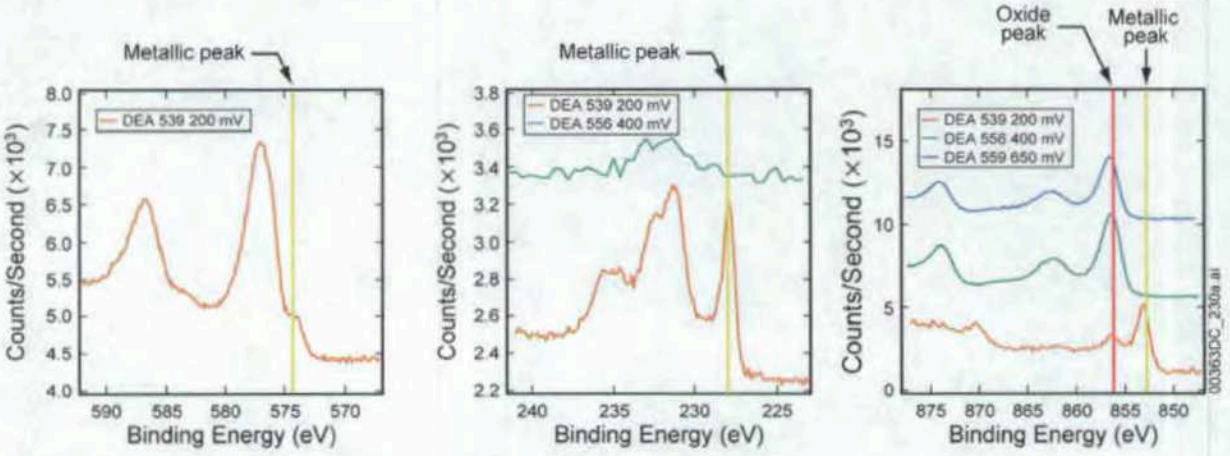

Source: LLNL 2003b.

NOTE: The figures show the Cr2p, Mo3d, and Ni2p regions from left to right. These spectra show that the surface oxide changes from a predominantly Cr_2O_3 film to a NiO as the voltage is increased from 200 to 400 mV.

Figure 8. XPS Spectra of Samples Held at Various Voltages in pH 8 Solution.

3.3 Experimental Evaluation of the Oxide that Forms under Basic Conditions

To determine the character of the oxide exposed to a basic solution, several samples were potentiostatically held in the passive region at 250 mV in BSW for 16 to 20 hours at a temperature of 90°C. An image of the oxide is shown in Figure 9. The oxide has a compact layer close to the metal and a porous outer layer. In basic solution (pH of approximately 12.5), the glass electrochemical cell partially dissolves, adding silica to the solution. The porous region is likely a silica deposit from the glassware. This was especially apparent when examining samples tested in simple NaCl/NaOH solution. The dissolved glassware formed thick silica deposits on the sample surface, precluding any surface characterization. Silica surface deposits are also observed on Alloy 22 specimens exposed in the LTCTF to silica-containing waters.

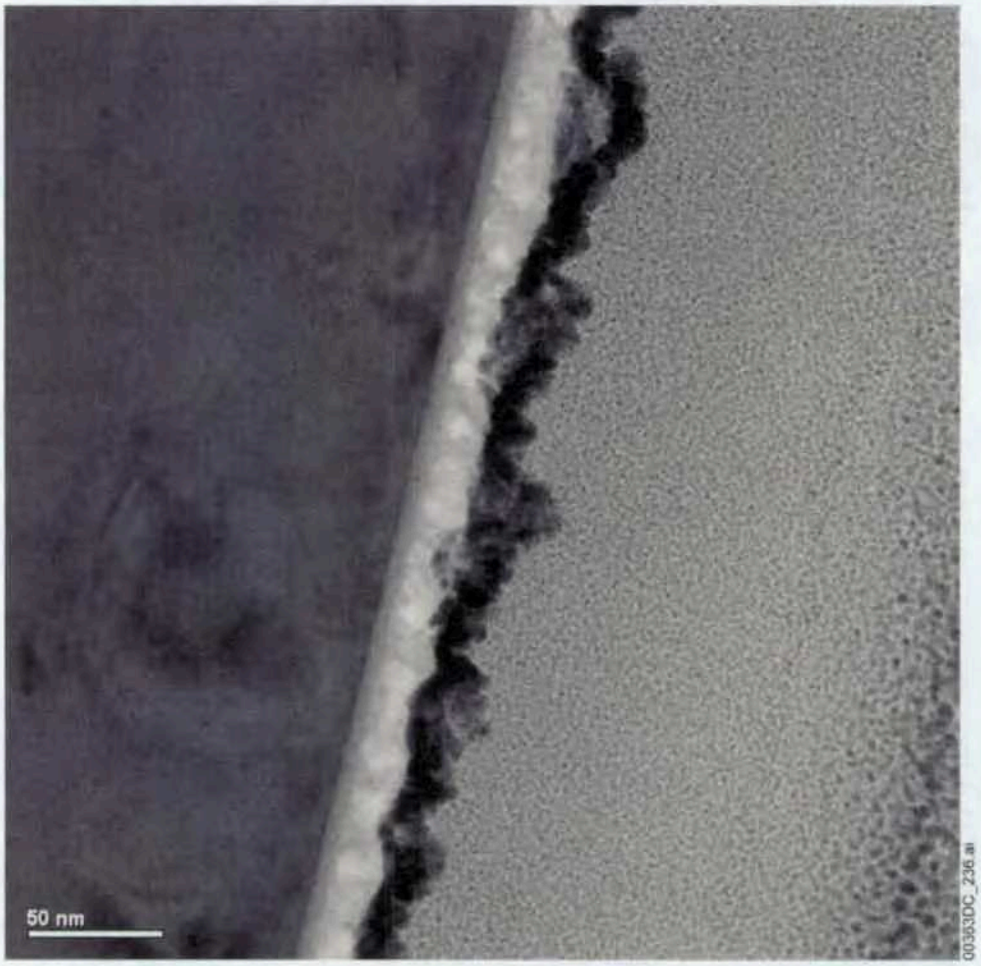

Source: DTN: LL040308412251.081.

NOTE: This TEM image shows the base metal at the left hand side of the image, the darkest layer is a gold-palladium coating deposited during the sample preparation process. The area between the Alloy 22 substrate and the gold-palladium coating is the region of interest. It is composed of an approximately 6 to 7 nm compact oxide close to base metal and a thicker, porous (light) region. The porous oxide is thought to be a silica scale.

Figure 9. Cross-Sectional TEM Image of Sample DEA496.

XPS depth profiling was used to determine the metal and oxygen composition across the oxide. The intensity versus sputter time is shown in Figure 10a. The intensities were normalized by the elemental sensitivity factors for each energy range. Unfortunately, high-resolution silicon windows were not added to the XPS depth profile, so the silicon composition cannot be seen as a function of depth. However, the low-resolution scan obtained prior to starting the depth profiling showed the presence of silicon at the surface. Because a major constituent is missing, the intensities were not converted to atomic concentrations.

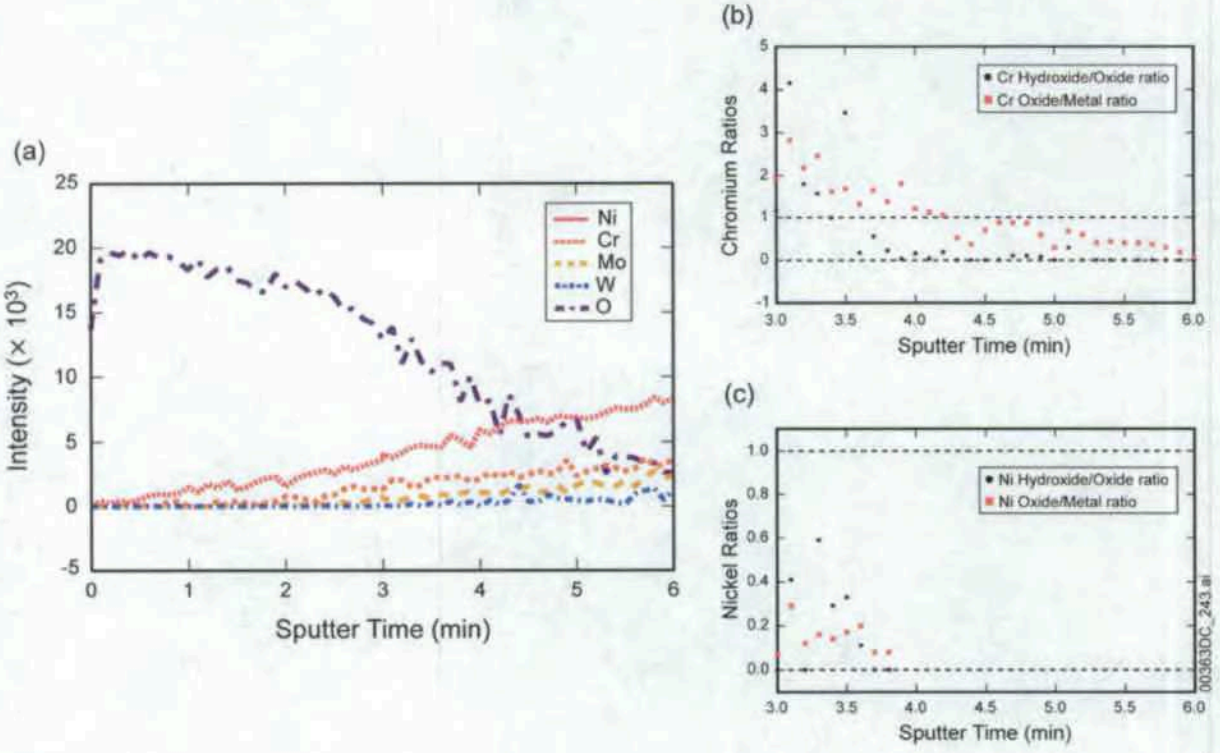

Source: DTN: LL040501112251.094.

Figure 10. (a) XPS Depth Profile across the Surface Oxide on Sample DEA465; Ratios of the Atomic Concentrations in the chromium (b) and nickel (c) Regions

At the deepest sputter point (6 minutes), the spectra have metal peaks but the metal concentrations have not yet leveled off to constant values as expected for the base metal. Also, the oxygen intensities are almost zero. Both of these points suggest that the sputtering has just crossed the oxide but has not penetrated deeply into the metal yet. The first half of the profile is dominated by the porous oxide, which is attributed to silica scale. The second half of the profile contains the compact oxide layer at the metal surface. In this second region, the chromium and nickel regions were fit to determine the relative contributions of the hydroxide, oxide, and metal species. The chromium ratios (Figure 10b) show that the oxide to metal ratio is greater than one midway through the sputtering and, as expected, trends to zero at the metal interface. In the range where chromium oxide exists (i.e., where the oxide to metal ratio is greater than one), the hydroxide to oxide ratio varies from greater than one to near zero. The nickel peaks were also fit (Figure 10c), but the hydroxide and oxide components were too small to be fit over the entire range. As found in the chromium speciation, more nickel hydroxide was found in the regions

farther from the metal. Taken together, these ratios suggest that the oxide at the metal surface is predominantly chromium oxide with some nickel. The oxide surface away from the metal has a hydroxide component.

3.4 Summary of Oxides Formed as a Function of pH and Applied Potential

In all environments tested, a stable, conformal oxide was formed that passivated the surface, preventing active dissolution of the metal. The oxides were dense and compact with strong adhesion to the surface and, due to this fact and the small thicknesses involved (2 to 5 nm), were mechanically stable and did not spall. The exception to this is a thick porous nickel oxide, which formed at higher potentials overlying a dense chromium oxide layer in solutions near pH 8 (±0.5). However, the passivity of the metal is due to the chromium oxide inner layer. If the porous layer were to spall off, this would have no effect on the passivity of the metal. In all of the environments studied, a dense, conformal, predominantly chromium oxide adheres to the metal surface. This oxide provides stability for the metal in the tested environments.

Near pH 3 (±0.4), the oxide is a thin (about 4 nm thick) conformal layer. At higher potentials within the passive plateau, the oxide becomes thinner but more compact and uniform. The oxide is predominantly chromium with some molybdenum, nickel, and tungsten.

At pH near 8 (±0.5), the oxide in the passive region is similar to that found in the acidic region; it is mostly chromium oxide with lower concentrations of molybdenum and nickel. At higher voltages, the oxide transforms into a film with two distinct layers, with a compact oxide (about 4 nm thick) near the surface and a porous structure (between 30 and 40 nm thick) at the oxide–solution interface. The outer porous oxide is almost entirely nickel oxide with some iron oxide. Similar oxide films were formed in SCW (DTNs: LL030300912251.036 and LL030301412251.038).

At basic pH, the surface has a coating of porous silica scale due to dissolution from the glassware. However, silica is present in a range of relevant brines and is observed to precipitate out of solution at the oxide–solution interface. The oxide underlying the silica is compact and is composed primarily of chromium oxide. In all cases, it appears that an amorphous Cr(III) oxide is responsible for the passive behavior of the metal.

4. THE EFFECT OF AGING IN SOLUTION

A series of surface studies were undertaken to evaluate the oxide evolution as a function of time. Surface evaluation was not anticipated prior to the start of these experiments. Rough, as-received coupons (rather than polished samples) were emplaced in the aging tanks and autoclaves discussed below in this section. The experiments were conducted in complex multi-ionic waters that were supersaturated with respect to carbonate and silica allowing scales to form on the coupons. These factors limited the assessment of the metal-oxide of interest in passivity. These issues were remedied in subsequent experiments described by Orme 2005.

4.1. Surface Evolution After Five Years in Multi-ionic, Concentrated Pore-water Solutions

Samples from the long-term corrosion test facility (LTCTF) were characterized to determine the oxide at the surface. Segments of four Alloy 22 "u-bend" samples were examined using cross-sectional transmission electron microscopy (TEM) and electron energy loss spectroscopy (EELS). The samples tested were, a non-immersed control and samples immersed in simulated acidic water (SAW), simulated concentrated water (SCW), and simulated dilute water (SDW) at 90°C for 5+ years (see DTN: LL041100112251.124 for details of the solution compositions). The primary finding is that the oxide remains thin (<5nm) after exposure to these environments.

The objective of this study was to characterize the passive oxide composition and thickness after aging in solution. However, all of the immersed samples had unintentional 100-5000nm deposits on their surfaces that came from carbon that leached from the walls of the tanks and/or iron that leached from other metals in the tanks. This oxygen containing contaminant layer severely limited the characterization of the passive oxide film. Depth profiling techniques such as XPS, Auger, or time-of-flight-SIMS that obtain elemental concentrations as the surface is sputtering, can not be used effectively on samples such as these where information is required from a *thin* (1-2nm thick), *buried* oxide at a *rough* metal interface, particularly, as common elements are found in the contaminant, the oxide, and the metal. The lack of contrast is also an issue for evaluation by EELS maps, however an upper bound can be estimated by comparing common features. The results from the control, and the SAW, SCW, and SDW solutions are discussed in turn.

The non-immersed control (Figures 11 and 12), like the mirror-polished samples shown in previous sections, has a very thin starting oxide. This contrasts the ~50nm thick oxide of the mill-annealed substrates and is presumably due to the fact that the U-bend samples have a RMS 32 finish, which removes thick oxides that may form during earlier phases of the manufacturing process. The processing also effects the base-metal, which is deformed and polycrystalline as indicated by the presence of rings in the diffraction pattern (Figure 11b). Electron Energy Loss Spectroscopy (EELS) maps (Figure 12) show a high carbon concentration, no nickel, and some oxygen, which suggests that the metal has a hydrocarbon film at its surface. While it is likely that there is a metal-oxide film, it is not evident from these micrographs, which suggests that it is quite thin (a few nanometers in thickness).

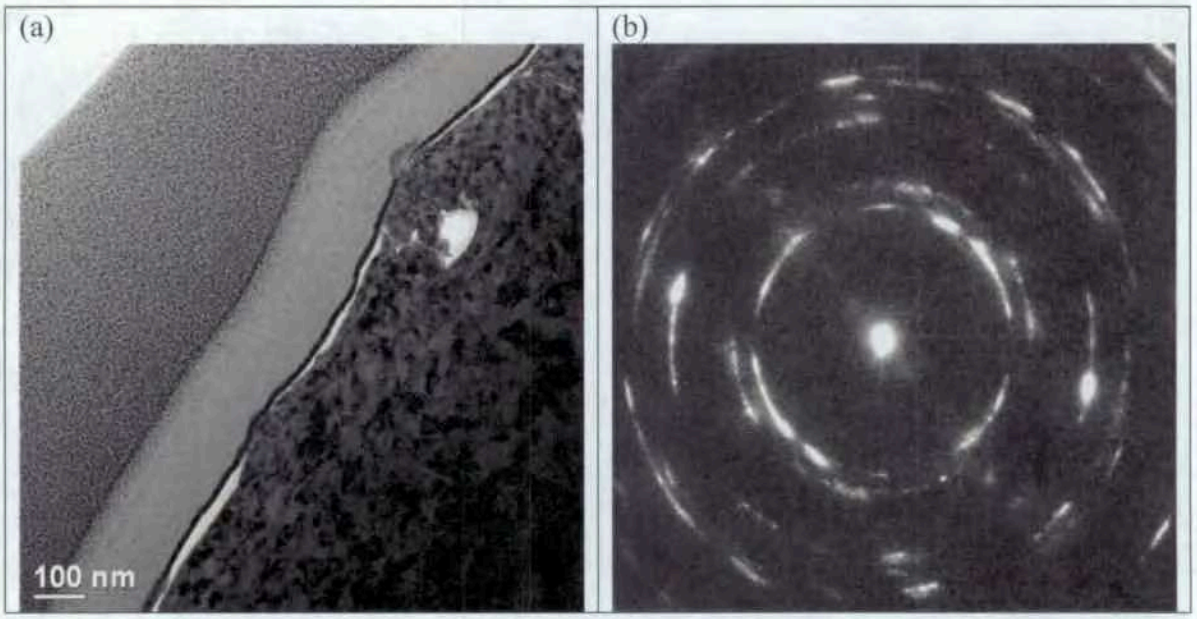

Source: Orme 2003b (p. 35); DTN: LL040308412251.081: (a) BF0003-labels.tif; (b) DP0007.tif. BF0003.tif (no labels) is in the DTN. BF0003-labels.tif is depicted on p. 36 of Orme 2003b.

Note: TEM image (a) at 23kx magnification. The gold and platinum are due to the sample preparation process. The gold marks the outer layer of the sample. The base metal is in the lower right corner. (b) A diffraction pattern from the base metal area. The streaks indicate that the substrate is deformed presumably from the mill processing steps

Figure 11. Cross-sectional TEM image and diffraction pattern of control sample (DUA160).

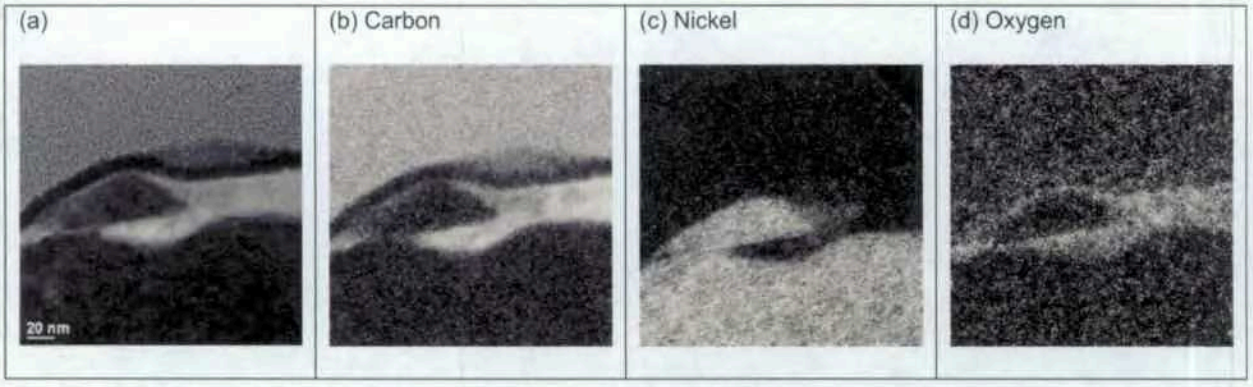

Source: Orme 2003b (p. 35); DTN: LL040308412251.081: (a) BF0015.tif (without the size scale in the lower left-hand corner); (b) "Carbon map.tif"; (c) "Nickel map.tif"; (d) "Oxygen map.tif).

Note: (a) TEM image with the base metal at the bottom. The dark gold layer marks the sample edge. The (b) carbon map, (c) nickel map, and (d) oxygen map indicate that the space between the gold and the base metal is a hydrocarbon rather than an oxide. This does not rule out a very thin oxide at the metal interface however it cannot be resolved from these images.

Figure 12. Image and elemental maps of control sample (DUA160) obtained at 125kX magnification.

The sample held in acidic SAW solution for over 5 years (Figure 13) has a thick, 0.2μm-0.4μm, wavy iron oxide scale. It is thought that this scale deposits from the solution rather than being a corrosion product. Several holes are also evident. The larger elliptical holes are ~0.2μm x 0.4μm. The source of these holes is unknown. However, the elemental maps shown in Figure 14 show that a 0.05- 0.1μm coat of carbon surrounds the holes. It is possible that these are dust particles that became coated with oil (from the mill processing steps) and then fall out during the sample preparation process. It is also possible that the voids represent sites where bacteria once existed. If the voids do represent bacteria than the carbon coating may be biogenic. As with the control sample above, there is a conformal, carbon and oxygen rich layer directly at the metal interface but no obvious metal-oxide. The metal interface looks smoother than the control sample, which may be an indication of corrosion. However, as noted in Section 6 the weight-loss samples from this tank have very low corrosion rates.

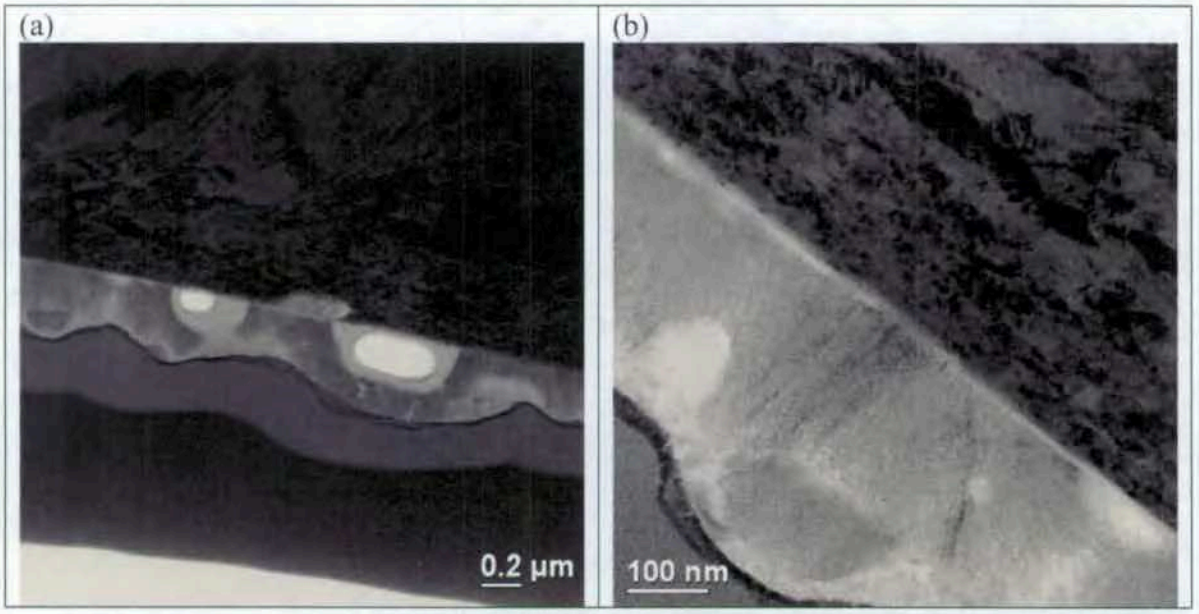

Source: Orme 2003b (p. 38); DTN: LL040308412251.081: (a) BF0101.tif (without the size scale), (b) BF0112.tif (without the size scale).

Note: (a) TEM image at 8.8kx magnification. The gold layer marks the surface and the base-metal is at the top of the image. In the region of interest between the gold and the base-metal there is a wavy iron oxide scale with voids. (b) A higher magnification image (37kx) showing the dark gold layer, the wavy iron-oxide scale, and the base-metal. Although SAW does not contain iron, non-Alloy22 racks within the LTCTF tank corroded over time. It is thought that the iron from the dissolution of the rack metals is responsible for the iron-oxide scale on the Alloy 22 samples. The source of the voids within the iron-oxide is not yet known.

Figure 13. Cross-sectional view of LTCTF sample held in SAW at 90°C for 5+ years (DUA054).

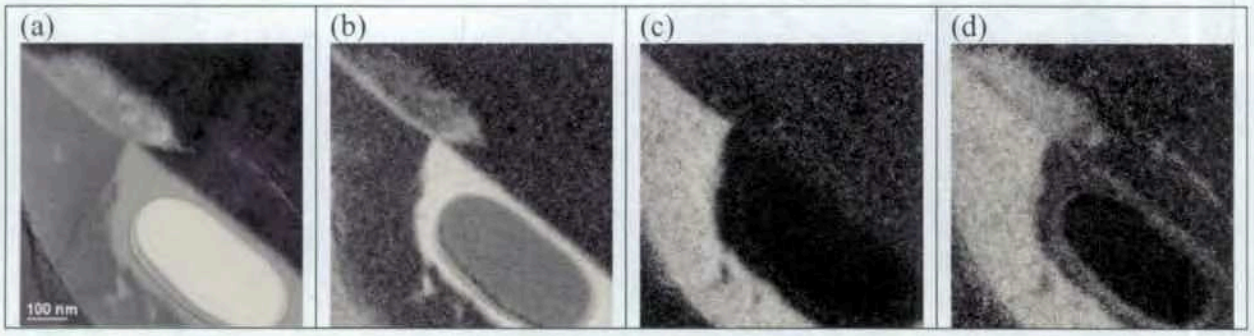

Source: Orme 2003b (p. 38); DTN: LL040308412251.081: (a) BF0107.tif (without the size scale); (b) "Carbon map0107.tif"; (c) "Iron map-0107"; (d) "Oxygen map-0107"

Note: (a) TEM image at 37kx magnification showing the region between gold and base-metal in the neighborhood of one of the voids. Electron energy loss spectroscopic (EELS) maps of this same area showing (b) carbon, (c) iron, and (d) oxygen. The voids are surrounded by a carbon layer.

Figure 14. Image and elemental maps of LTCTF sample held in SAW at 90°C for 5+ years (DUA054).

Sample DUA114 was immersed for 5+ years in the LTCTF in 90°C SCW. Images of the sample surface are shown in (Figure 15-16). The surface has a 50-150nm thick "wavy" carbon film at the metal interface. The sample held in SDW at 90°C for over 5 years (DUA140) looks similar to the sample held in SCW, although the carbon deposit is somewhat thicker (Figures 17-18). In both cases, it is likely that the carbon deposits are due to the partial dissolution of the tank linings in these basic solutions.

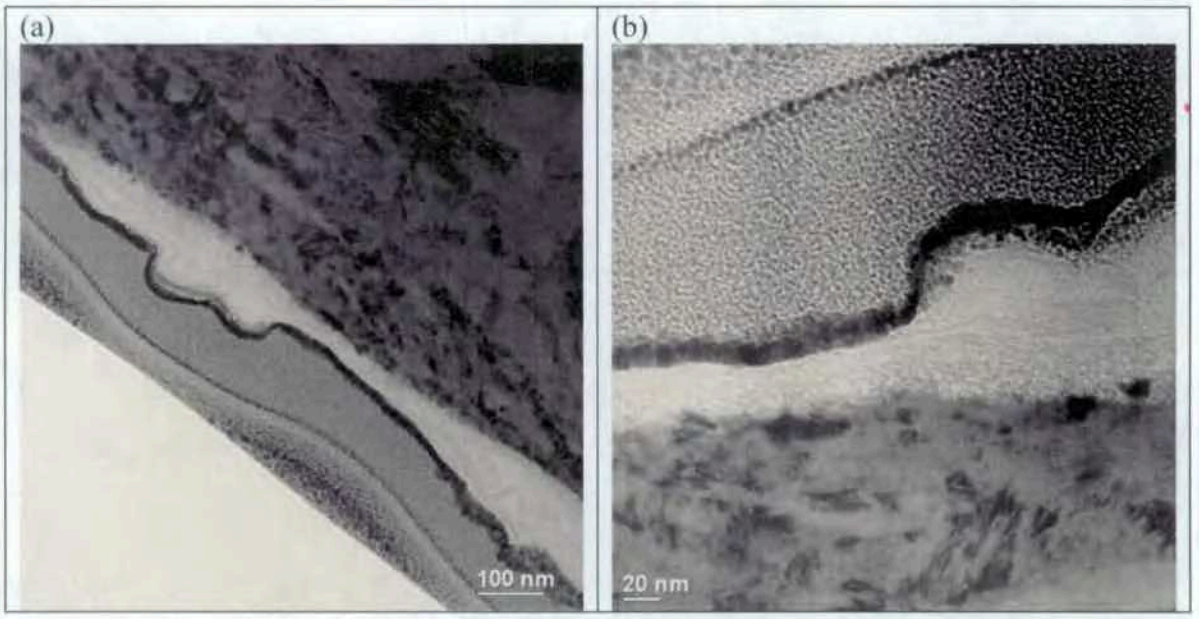

Source: Orme 2003b; DTN: LL040308412251.081: (a) BF0211.tif (with the size scale in the lower left-hand corner); (b) BF0212.tif (with a 40 nm size scale present).

Note: (a) TEM image at 20kx magnification. A scale bar in the lower left corner shows a 100nm length. The gold layer marks the surface and the base-metal is at the upper right. In the region of interest between the gold and the base-metal, there is a wavy carbon deposit ~150nm wide at its thickest regions. There are two morphologies; one thin conformal layer next to the metal and the other thicker and less homogeneous. (b) A higher magnification image (59kx) showing the dark gold layer, the wavy carbon deposit, and the base-metal. It seems likely that the thin conformal carbon layer is due to the as-received condition of the sample and that the thicker carbon layer is due to partial dissolution of the LTCTF tank linings

Figure 15. Cross-sectional view of LTCTF sample held in SCW at 90°C for 5+ years (DUA114).

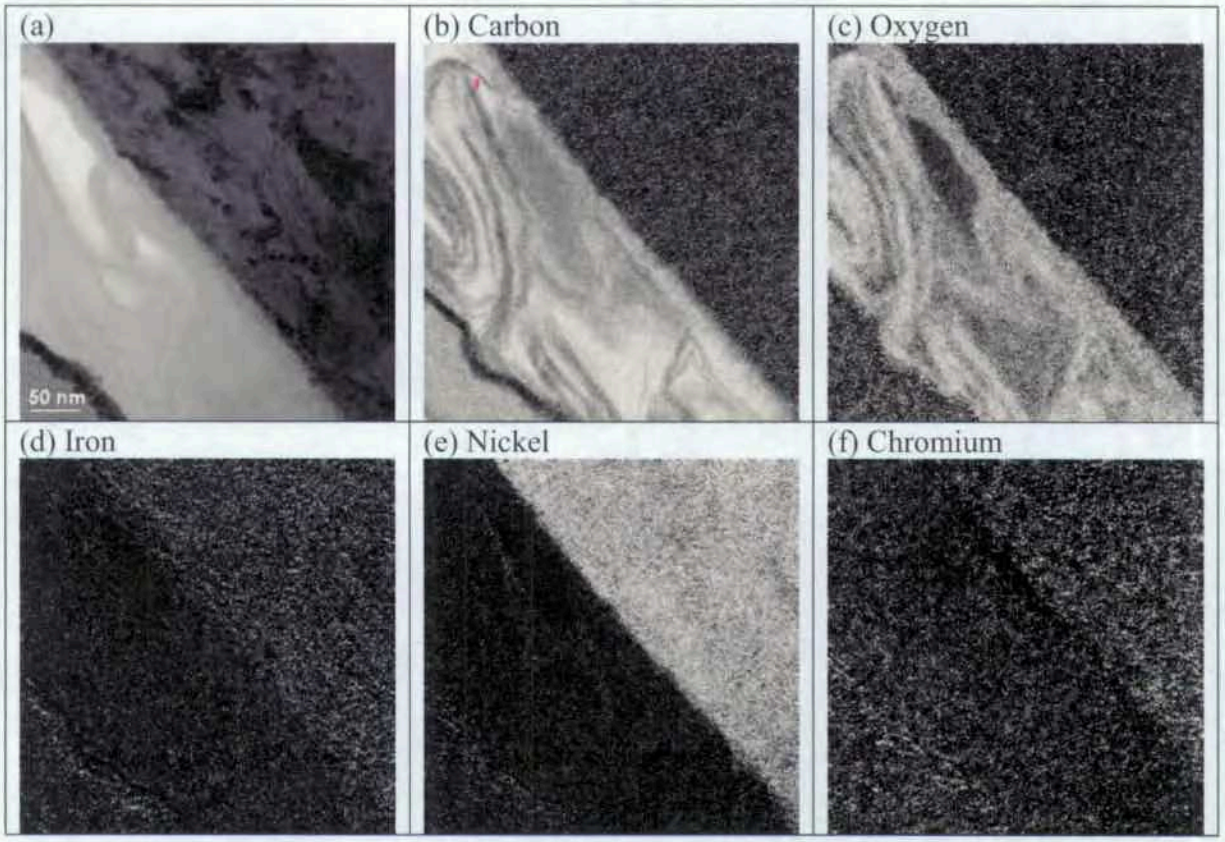

Source: Orme 2003b; DTN: LL040308412251.081: (a) BF0243.tif; (b) "Carbon map-0243.tif"; (c) "Oxygen map-0243.tif"; (d) "Iron map-0243.tif"; (e) "Nickel map-0243.tif"; (f) "Chromium map-0243.tif".

Note: (a) TEM image at 72kx magnification showing the region between the gold and base-metal. Electron energy loss spectroscopic (EELS) maps of this same area showing (b) carbon, (c) oxygen, (d) iron, (e) nickel, and (f) chromium. This region is composed of carbon and oxygen with no appreciable metal content.

Figure 16. Image and elemental maps of LTCTF sample held in SCW at 90°C for 5+ years (DUA114).

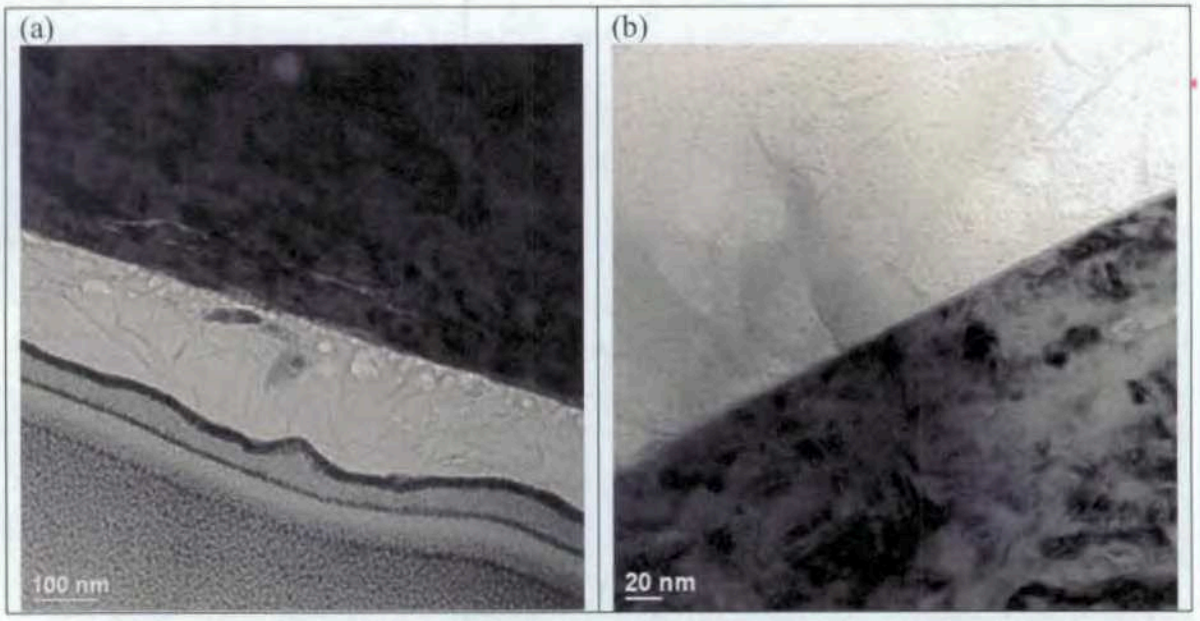

Source: Orme 2003b; DTN: LL040308412251.081: (a) BF0307.tif; (b) BF0312tif (with a 40 nm size scale present).

Note: (a) TEM image at 20kx magnification. A scale bar in the lower left corner shows a 100nm length. The gold layer marks the surface and the base-metal is at the upper right. In the region of interest between the gold and the base-metal, there is a wavy carbon deposit ~250nm wide at its thickest regions. (b) A higher magnification image (59kx) showing the dark gold layer, the wavy carbon deposit, and the base-metal.

Figure 17. Cross-sectional view of LTCTF sample held in SDW at 90°C for 5+ years (DUA140).

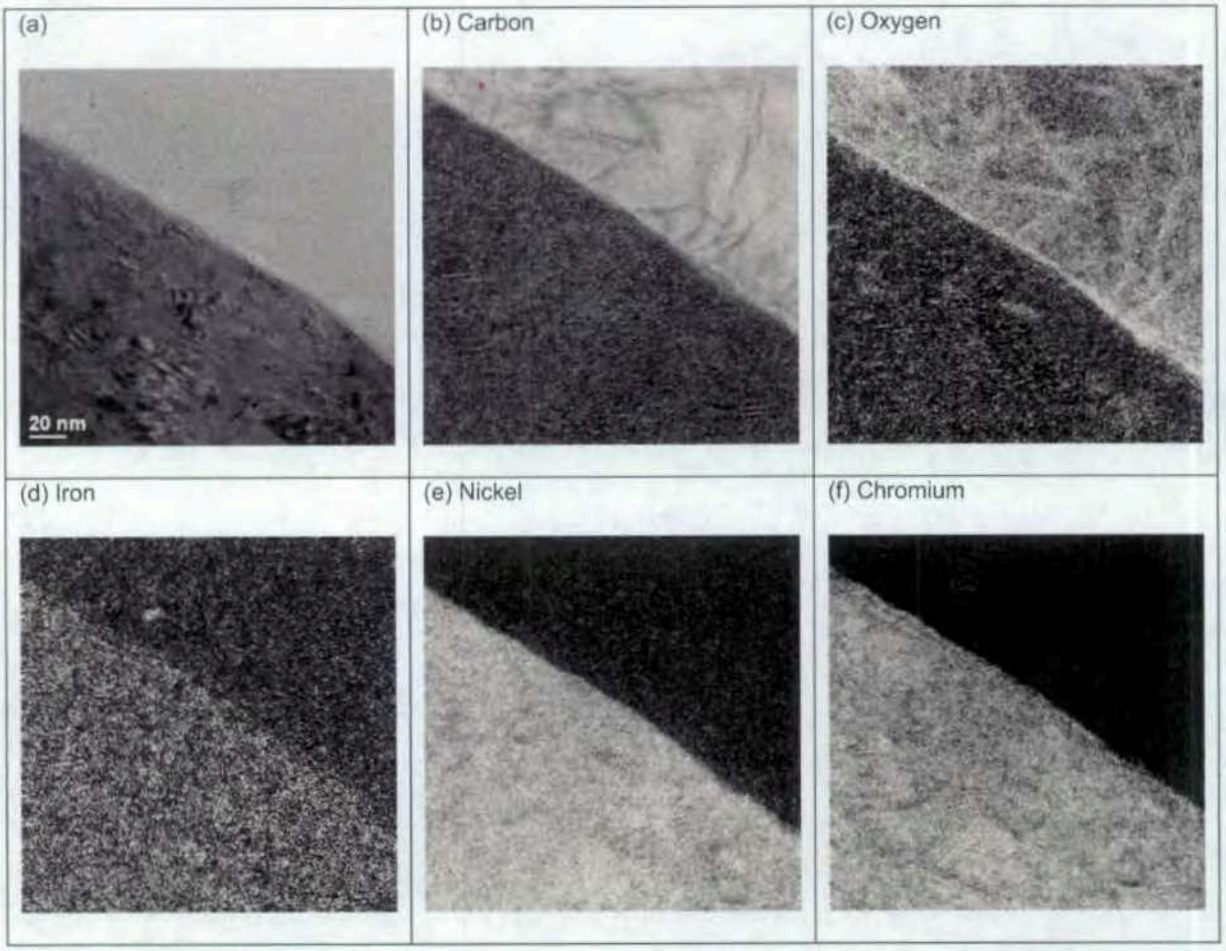

Source: Orme 2003b; DTN: LL040308412251.081: (a) BF0337.tif (without the size scale included above); (b) "Carbon map-0337.tif"; (c) "Oxygen map-0337.tif"; (d) "Iron map-0337.tif"; (e) "Nickel map-0337.tif"; (f) "Chromium map-0337.tif".

Note: The base-metal is at the lower left corner of each image. The deposit is primarily carbon and oxygen with no appreciable nickel, iron or chromium. The oxygen map shows a thin conformal layer at the metal interface. This appears to be a hydrocarbon rather than a metal-oxide.

Figure 18. (a) TEM image and (b)-(f) electron energy loss (EELS) maps showing the metal interface for a sample held in SDW at 90°C for 5+ years (DUA140).

The primary finding from these experiments is that the metal-oxide does not thicken appreciably with time in the environments tested. While a thin oxide is presumed to exist at the metal interface (due to the low corrosion rates from weight-loss), the exact nature of the oxide could not be determined due to the interference from other carbon and iron deposits.

4.2. Surface Evolution over 8-months in Silica Containing Basic Solutions

Additional characterization was performed on solution-annealed Alloy 22 samples aged in a less concentrated version of so-called Basic Saturated Water (CRWMS M&O 2000), which is

simulated Yucca Mountain ground water (J-13 well water) concentrated ~50,000-fold. The less concentrated solution (Table 4) used in these tests is BSW diluted to yield ~2800-fold J-13 and has a pH of ~12.4 at the test temperature of 95°C.

Table 4. Chemical composition of concentrated (~2800-fold) Yucca Mountain J-13 well water.

10.6 g Na_2CO_3 (anhydrous)	9.7 g KCl
8.8 g NaCl	0.2 g NaF
13.6 g $NaNO_3$	1.4 g Na_2SO_4 (anhydrous)
4.1 g Na_2SiO_3*$9H_2O$	1000 g H_2O

Source: Kim 2004 (Table 1).

Samples were removed after 1, 2, and 8 months to evaluate the surface oxide composition and thickness. Figure 19 shows the TEM cross-section micrograph of the oxide film formed for 2 months on Alloy 22 in the mixed-salt solution at 95°C. After exposure to solution, an approximately 5-8 nm thick oxide is found. Electron diffraction spectroscopy (Figure 19b and 19c) shows that the oxide contains chromium, oxygen, and nickel, consistent with Cr_2O_3 mixed with nickel. The initial surface was not characterized. It may have resembled Figure 32, which is an as-received solution-annealed sample or it may have resembled Figure 11 which is a solution annealed surface followed by a polish that removed the oxide. Without firm knowledge of the starting surface it is difficult to state whether the oxide seen in Figure 19 represents the growth or partial dissolution of a Cr-Ni oxide.

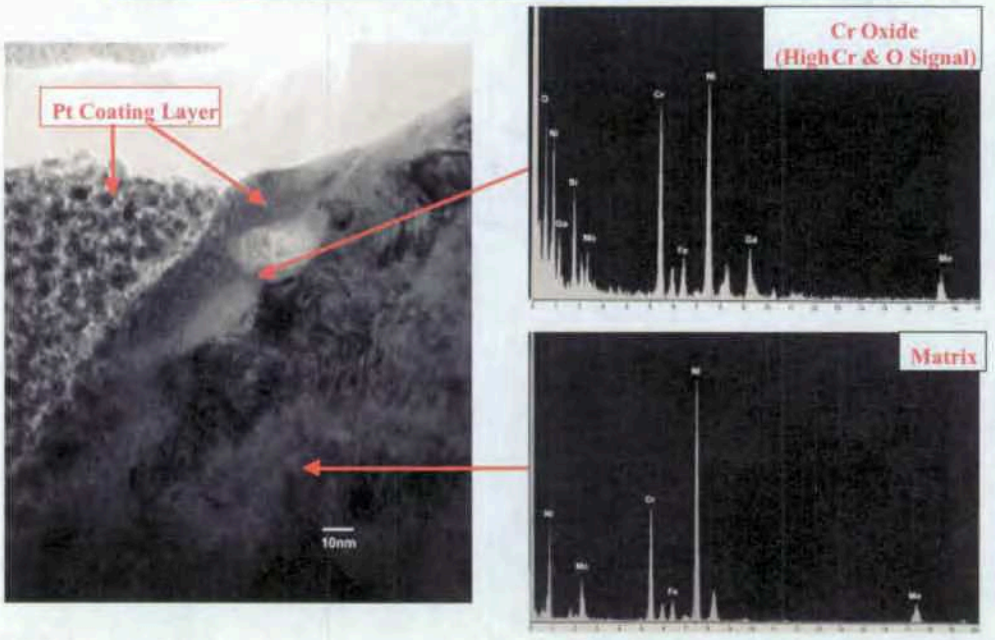

Source: Kim 2004 (Figure 1, p. 5).

Figure 19. TEM micrograph showing the cross-section views and oxide chemistry formed on Alloy 22 for two months at 95 °C in a mixed-salt environment.

XPS analysis was performed for quantitative chemical profiles of the oxide thickness and elemental distribution through the oxide film. Figure 20 shows the XPS elemental distribution of the oxide layer formed on Alloy 22 as a function of immersion time. The oxide film on Alloy 22 was enriched with Cr and Ni. However, a large amount of SiO_2 with various salts on the outer oxide film was detected, but no evidence of penetration of SiO_2 to the underlying substrate was observed. This is consistent with Figure 9, which shows two distinct layers as silica forms on a polished sample.

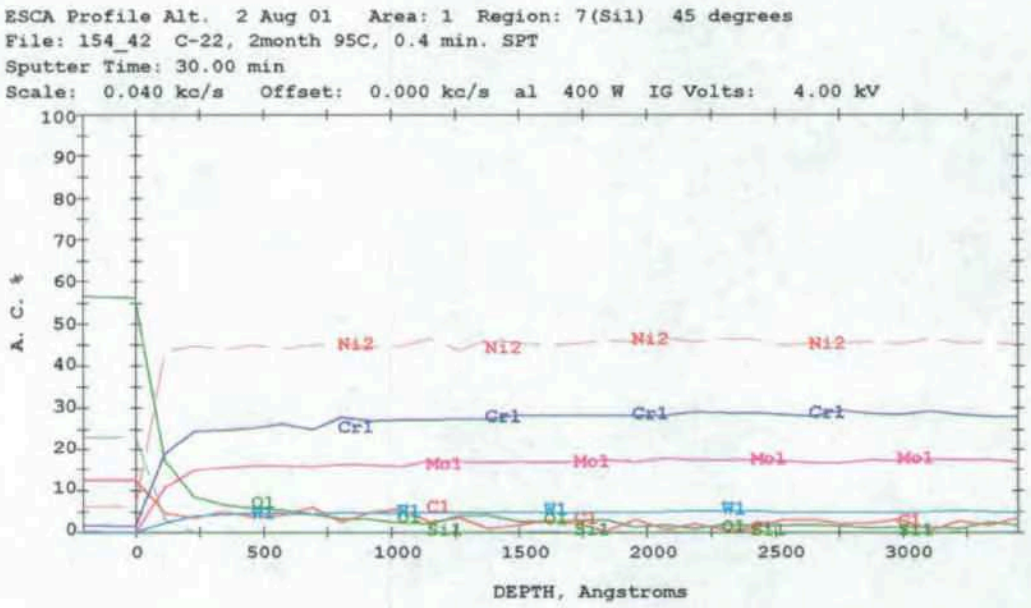

Source: Kim 2004 (Figure 2, p. 5).

Figure 20. Elemental depth profile on oxide layer formed on Alloy 22 for 2 months in a mixed-salt environment at 95°C.

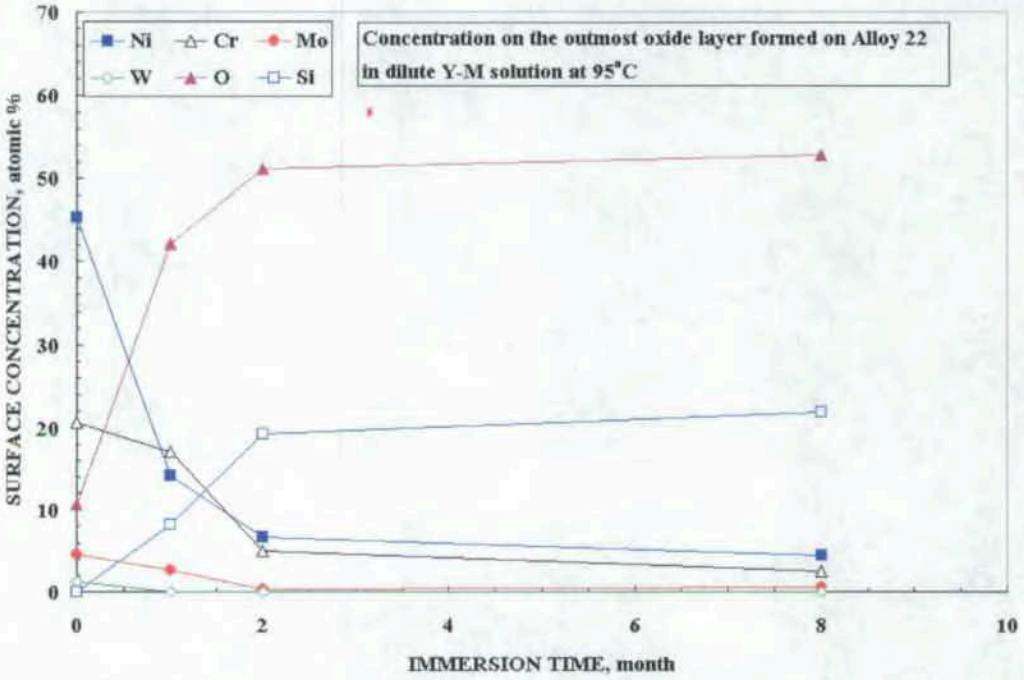

Source: Kim 2004 (Figure 7, p. 8)

Figure 21. Elemental concentration on the outmost oxide layer (before removing impurities) formed on Alloy 22 at 95°C in a mixed-salt environment as a function of immersion time.

The primary finding is that silica grows on the surface when the solution is supersaturated with respect to silica. This obscures any information about the passive oxide.

5. OXIDE GROWTH RATE

The kinetics of passive film growth on metals are often investigated by following the decay of the anodic current (i) with time (t) upon potentiostatic polarization in the passive region (MacDougall 1983; Bulman and Tseung 1972). In general, the thickness of a film is proportional to the anodic charge (Q). The rate of film growth at a constant potential decreases exponentially with increasing thickness, such that an expression of the form:

$$i = Ae^{(-\%)}, \qquad \text{(Eq. 1)}$$

where A and B are constants that depend on parameters of the film, describes the relationship between current and film thickness. By taking the logarithm of both sides of Equation 1, it is found that $\log(i) \propto Q$. Therefore, if the film growth is indeed logarithmic, a plot of $\log(i)$ versus $\log(t)$ should be linear.

Despite considerable work that has been carried out and the available literature describing the formation of anodic oxide films on metals, no universally accepted model has been devised to explain the mechanism of anodic oxide growth. However, two theories: the high field model and

the point defect model, have been advanced to account for the properties of experimentally observed anodic passive films.

Quantitative descriptions of the kinetics of film formation date back to the work of Cabrera and Mott (1949). The most basic approach assumes that ion transport through the film is controlled by the electric field across the film. The higher that the field is, the lower the activation energy for ion or vacancy hopping is (this is called the high-field mechanism) (Bulman and Tseung 1972). Consequently, the rate determining reactions can be attributed to the potential difference between the metal–oxide interface (Cabrera and Mott 1949) and the oxide–environment interface (Fehlner and Mott 1970). When the electric field at the surface can no longer reduce the activation barrier for diffusion, the oxide reaches a limiting thickness value.

The point defect model has also been proposed to explain the kinetics of passive film growth (Macdonald 1999). According to the model, the anodic current that passes after the first few seconds of passivation is mainly associated with breakdown at local weak points in the oxide film and subsequent anodic repassivation. Repassivation involves both reformation of the oxide and metal dissolution. Since the current is a measure of the resistance of the oxide toward local breakdown, its logarithmic decrease with time suggests a logarithmic increase in the state of perfection of the oxide film (MacDougall 1983).

In Figure 22, log(i) versus log(t) plots are shown for anodic oxide growth on Alloy 22 in pH 7.5, 1-mol/L NaCl solution at 90°C for various potentials. For each measurement, the potential was changed instantaneously from the open circuit potential to the indicated potential and the decay of i was subsequently monitored for approximately 16 hours. The extent of linearity of the log(i) versus log(t) plot is indicated by extrapolating the initial readings to longer polarization times (as indicated by the dashed line in Figures 22 and 23). At a potential of 150 mV versus Ag/AgCl, the log(i) versus log(t) relationship is approximately linear for the duration of the experiment time. At potentials of 400 and 700 mV, the current after a long time (10^4 seconds) eventually deviates from the linear behavior (DTN: LL040501012251.093).

In Figure 23, log(i) versus log(t) plots are shown for Alloy 22 in pH of 2.8, 1-mol/L NaCl solution at 90°C at potentials of 200 mV and 500 mV. At both potentials, the curve deviates from linearity markedly earlier (10^3 seconds) than in the pH 7.5 solution. The results indicate that the cutoff time for the linear decrease of log(i) with log(t) increases with decreasing solution aggressiveness and increasing potential. MacDougall (1983) reports similar results for the passivation of nickel.

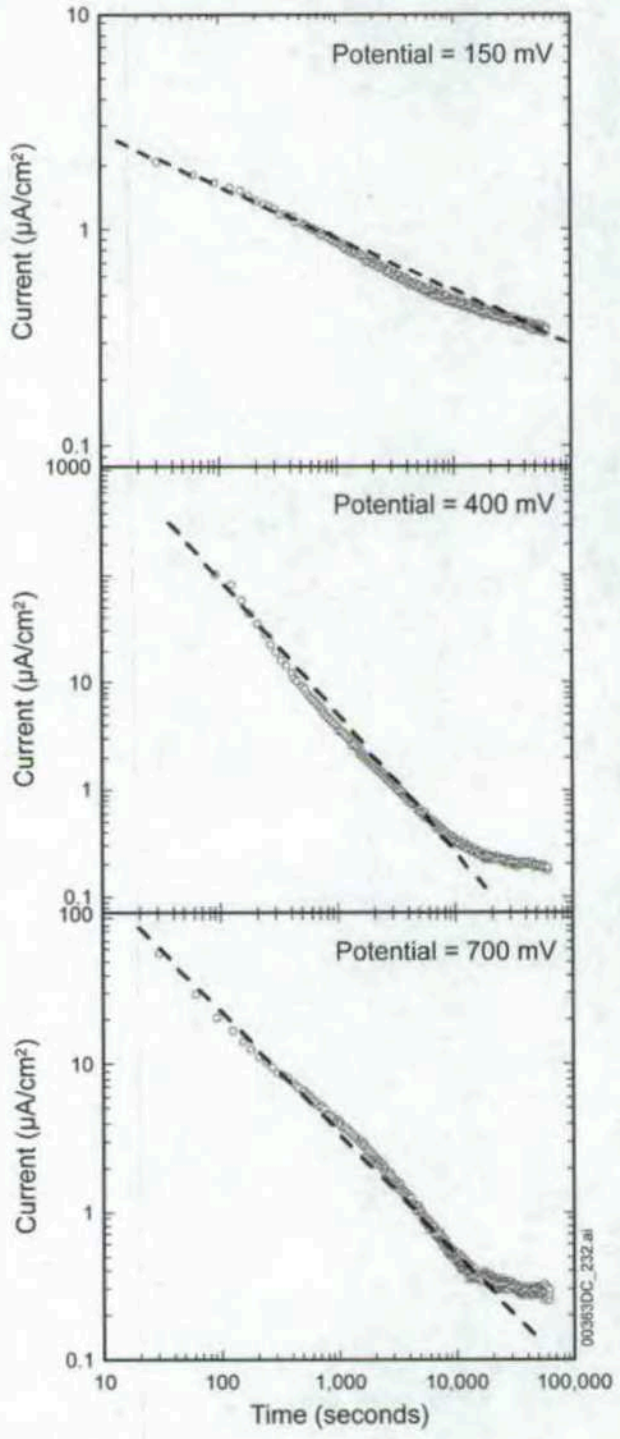

Source: DTN: LL040501012251.093.

Figure 22. Plots of log(i) versus log(t) for Alloy 22 in 1 mol/L NaCl with pH 7.5, at 90°C, at Potentials of 150 mV (top), 400 mV (middle), and 700 mV (bottom) versus Ag/AgCl

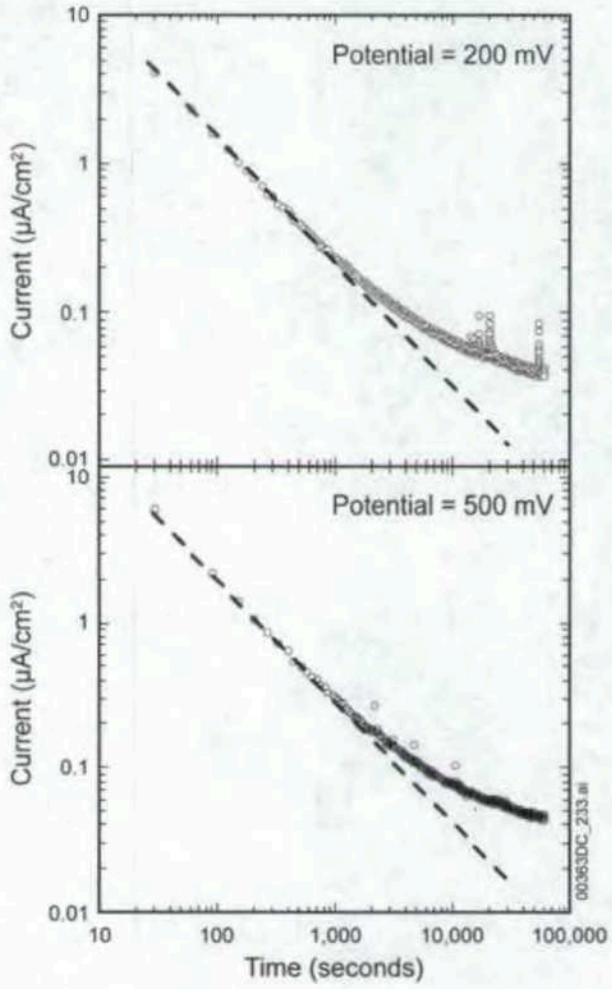

Source: DTN: LL040501012251.093.

Figure 23. Plots of log(i) versus log(t) for Alloy 22 in 1 mol/L NaCl with pH 2.8, at 90°C, at Potentials of 200 mV (top) and 500 mV (bottom) versus Ag/AgCl

The results for the passive film growth on Alloy 22 presented in Figure 22 and Figure 23 indicate that for a large portion of time, the relationship between log(i) and log(t) is linear. Consequently, the film growth is logarithmic. This claim is further substantiated by tests done at the LTCTF, which show films after 5 years in aqueous environments with similar thickness as those from the short studies presented. These films have strong adhesion to the surface, are mechanically stable, and show no evidence of spalling. The point defect model is therefore appropriate to model the observed results.

Deviations from linearity in log(i) versus log(t) have been discussed by MacDougall (1983) using the point defect model. The essence of the model is that oxide perfection (increase in stability) occurs at local defect sites, where dissolution and subsequent repassivation results in a more perfect oxide. The lifetime of the oxides at these sites depends on the aggressiveness of the solution and the applied potential. The logarithmic increase in film stability with time can be explained by the fact that the local oxide lifetime increases rapidly as the oxide becomes more perfect. In the early stages of passivation, the oxide is able to perfect itself easily because the

lifetimes required for an increase in local stability are short. Once the film reaches a higher level of perfection, longer dwell times are required for a further increase in perfection. Oxide dwell times are longer in less aggressive solutions (e.g., pH 7.5, 1 mol/L NaCl), thus, the oxide can achieve a very high state of perfection. Deviation from linearity in the log(i) versus log(t) plot is only observed after long times of polarization (as in Figure 22). Conversely, in more aggressive solutions, localized chemical dissolution of the oxide is rapid, and the local dwell times are short, leading to a rapid increase in oxide perfection and, therefore, early deviation from linearity in log(i) versus log(t). Eventually, a steady state may be reached where no further increase in perfection can occur and the anodic current is thus constant in time (as in Figure 23).

In conclusion, the linearity of log(i) versus log(t) plots, in conjunction with data from the LTCTF, provides conclusive evidence that the passive oxide on Alloy 22 grows logarithmically with time. By utilizing the point defect model, physical insight into the kinetics of growth was gained. Deviations in the linearity of log(i) versus log(t) plots at longer times, in more aggressive solutions and higher potentials, were due to rapid chemical dissolution of the oxide enabling a steady state to be reached where the anodic current becomes constant in time.

6. OXIDE STABILITY AS A FUNCTION OF pH AND APPLIED POTENTIAL

To address the question of film stability, two electrochemical metrics are used: the polarization resistance and the current density after holding at fixed voltage for a time period. These are converted to a corrosion rate (or penetration rate) so that they can be compared. However, they do not all measure equivalent processes. The polarization resistance measurement provides an instantaneous corrosion rate, whereas the current density after 16 to 20 hours gives a value closer to the steady state corrosion rate. Neither of these will be the same as values obtained from weight-loss measurements, which integrates the corrosion rate over the history of the specimen. Nevertheless, within each metric, different environments can be compared. Because electrochemical results did not differ in the buffered and multi-ionic solutions, they are grouped in these data sets.

Polarization Resistance as a Metric–At open circuit potential, the polarization resistance can be measured. This in turn can be converted to a corrosion rate following guidelines set forth in ASTM G 59-97, *Standard Test Method for Conducting Potentiodynamic Polarization Resistance Measurements*. Most samples were held at open circuit potential for 24 hours prior to measuring the polarization resistance and thus reflect a surface that has partially equilibrated with the solution. The polarization resistance measures an instantaneous corrosion rate at this point in time. The open circuit potential and presumably polarization resistance continue to evolve over time, but the majority of the change occurs over the first 24 hours. The data are plotted against the pH of the solution in Figure 24a, and against the open circuit potential in Figure 24b. The average values and standard deviations for the base metal samples are 2.1 ±1.2 μm/yr, 0.3 ±0.3 μm/yr, and 1.5 ±0.4 μm/yr for pH 3, 8, and 11 respectively (DTN: LL040500812251.091). The average values and standard deviations for the weld metal samples are 1.0 ±0.5 μm/yr, 0.11 ±0.03 μm/yr, and 0.17 ±0.03 μm/yr for pH 3, 8, and 11 respectively (DTN: LL040607512251.109). The major findings are: (1) the average polarization resistance corrosion rate is higher in solutions near pH 3 and 11 than pH 8, (2) the welds do not differ significantly from the base metal, and (3) the corrosion rate does not trend with open circuit potential.

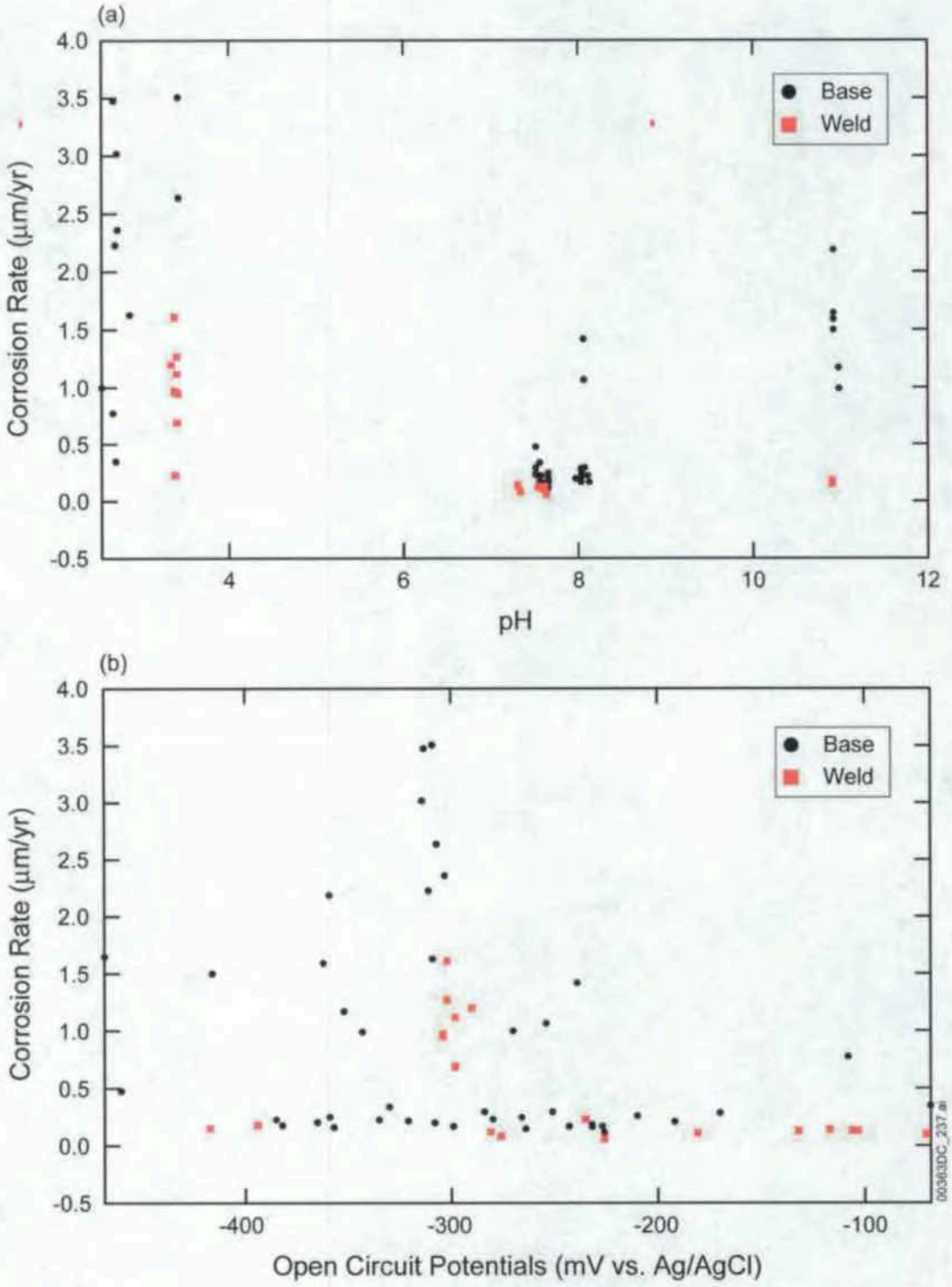

Source: DTNs: LL040500812251.091 and LL040607512251.109.

NOTE: The polarization resistance corrosion rate is plotted against pH (a) and (b) shows the open circuit potentials at which the tests were performed. Voltages are versus Ag/AgCl electrode.

Figure 24. Corrosion Rate as Determined by the Polarization Resistance Shown as a Function of the Solution pH.

Corrosion Rate from the Current–When Alloy 22 is held at fixed potential within the passive region, its current decreases over time. Figure 22 illustrates the current response as the metal equilibrates with a pH 7.5 solution. The current response has two regions: the first associated with oxide growth and the second associated with the steady state. The steady state current gives the balance between dissolution of the oxide and reformation of the passive film.

In this comparison, the current after 16 to 20 hours is converted to a corrosion rate using ASTM G 102-89, *Standard Practice for Calculation of Corrosion Rates and Related Information from Electrochemical Measurements*. In most cases, this time duration is sufficient for the current response to be beyond the quickly changing oxide growth region. In Figure 22, it can be seen that the sample held at 150 mV is still in the oxide growth region, whereas samples held at 200 mV (not shown), 400 mV, and 750 mV are not. However, the time duration may not be long enough for these values to reflect a true steady state current value. To determine this, these values would need to be compared with long-term tests.

Figure 25 shows the corrosion rates plotted as a function of pH and applied voltage. The average values and standard deviations for the base metal are 1.9 ±3.0 μm/yr, 2.0 ±1.7 μm/yr, and 1.9 ±1.6 μm/yr for pH 3, 8, and 11 respectively (DTN: LL040500712251.090). Too few weld metal samples were tested potentiostatically for meaningful statistical calculations. The four samples that were tested at pH 3 had final current corrosion rates below 0.31 μm/yr at both 200 and 400 mV potentials (two samples tested at each potential). At pH 8, the final current corrosion rates were below 0.8 μm/yr at both 200 and 400 mV potentials (two samples tested at each potential). Two samples were tested at 650 mV, which is approaching transpassive dissolution; one of the samples had a corrosion rate of 2.3 μm/yr, and the other had a corrosion rate of 21.2 μm/yr. This variation could be due to an experimental outlier or proximity of the transpassive region (DTN LL040607412251.108). The primary finding is that the corrosion rate does not show strong trends with either pH or voltages for the ranges tested. The pH values tested ranged from 3-12 and include buffered solutions as well as multi-ionic, SAW, SCW, and BSW. The basic solutions had silica deposition from the glassware. The voltages ranged from the open circuit potential to transpassive dissolution. It is interesting to note that even though samples in pH 8 solution have a phase transition that occurs at about 350 mV, the current response after 16 hours is approximately the same for the region with the thin oxide as well as the porous oxide (Figure 7). The data set also includes several measurements in the transpassive region; these data (at 750 mV and above) have much higher currents and are not shown on the graphs.

As was seen from the discussion of oxide characterization, chromium oxides with chromium in the 3+ oxidation state are the primary species in the barrier layer for the range of pH and potential values tested. The equilibrium speciation modeling suggests that the Cr_2O_3 that forms at pH 2.8, and the $NiCr_2O_4$ that forms at pH 7.5 may be thermodynamically stable. However, this was only shown for conditions where 1 g of metal was dissolved into 1 kg of NaCl solution. This corresponds to approximately 0.01 mol/L dissolved Alloy 22. In the experiments above, the measured currents provide an estimate of the metal transferred to solution. If the entire current is assumed to be due to metal dissolution, metal concentrations are 10^{-5} to 10^{-6} mol/L. At these concentrations, it is very unlikely that chromium oxides are thermodynamically stable oxide phase.

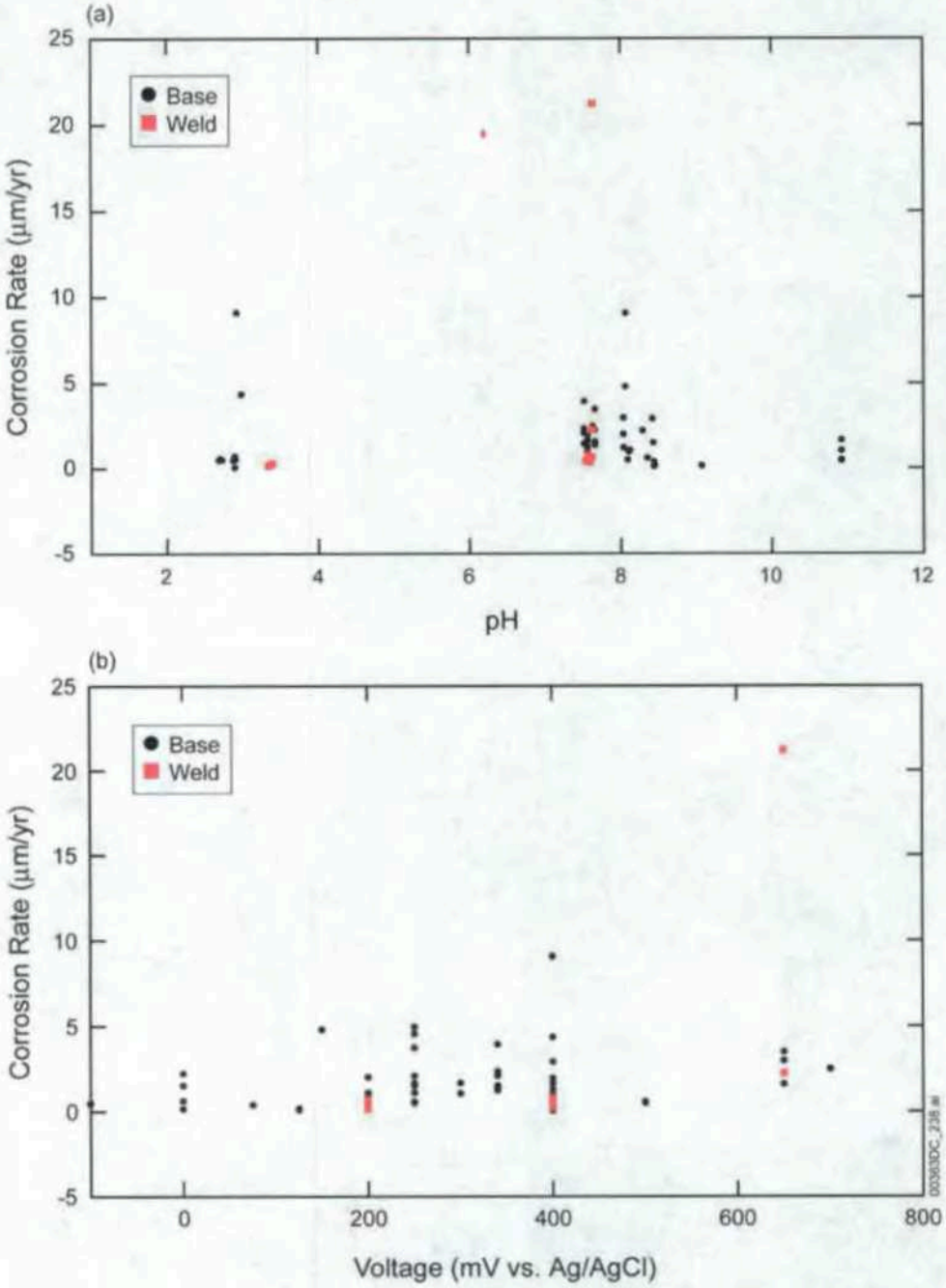

Source: DTNs: LL040500712251.090 and LL040607412251.108.

NOTE: The final current corrosion rate is plotted against (a) pH and (b) applied voltage. Voltages are versus Ag/AgCl electrode.

Figure 25. Corrosion rate (calculated from current) after Equilibrating at Constant Potential for 10 to 20 Hours.

In summary, the data show that the currents decay to the microampere range in 18 hours at all solutions tested between the OCP and transpassive dissolution. This implies that an oxide layer forms which inhibits current flow. The data also show that this barrier oxide is predominantly chromium oxide with a chromium(III) oxidation state. It seems unlikely that the oxide is thermodynamically stable given the low concentrations of metal in solution. Taken together, this suggests that a kinetically stable chromium oxide layer forms well before enough metal dissolves into solution to make the solution saturated with respect to the oxide phase. Presumably, if sufficient current were to flow or if the solution volume were small (as might be expected in vapor or water droplets on the waste package surface), then the solution would saturate and the oxide would become thermodynamically stable under fixed conditions.

Several reasons are provided in the literature for the stability of the passive film. Marcus and Maurice (2000) find that the grains of nanocrystalline Cr_2O_3 on Cr (110) have a surface of hydrated chromium hydroxide. They suggest that the hydroxide surface coating acts like cement to limit transport along grain boundaries. Some authors suggest that a bipolar oxide film forms with a net negative charge at the oxide–solution interface and a net positive charge at the metal–oxide interface. The negative net charge reduces the diffusion of negative anions to the oxide/hydroxide surface, and this in turn limits reactions with the metal that rely on anodic current flow. This picture is discussed by Schmuki (2002). The net charge on Alloy 22 has not been measured as part of this work.

If Cr_2O_3 is kinetically rather than thermodynamically stable, then it will dissolve at the surface, and chromium metal will be converted to chromium oxide at the metal–oxide interface. The initial oxidation creates a slight weight gain, but over time the surface dissolution will counteract that gain, and eventually a net weight loss will be observed. At the end of the test, the oxides and scales are removed from the surface of the samples, leaving the bare metal. This is weighed to ascertain the total weight loss due to corrosion. The LTCTF has had specimens in test for over 5 years in solutions with pH 3 to 11. Corrosion rates for both mill annealed and as-welded specimens can be determined from the mass loss. Thus far, the corrosion rates, which are shown in Figure 26, are between 10^{-3} and 10^{-2} μm/yr. This indicates that the general corrosion rate from the kinetically formed films under the conditions evaluated is sufficiently low to ensure the lifetime of the waste packages.

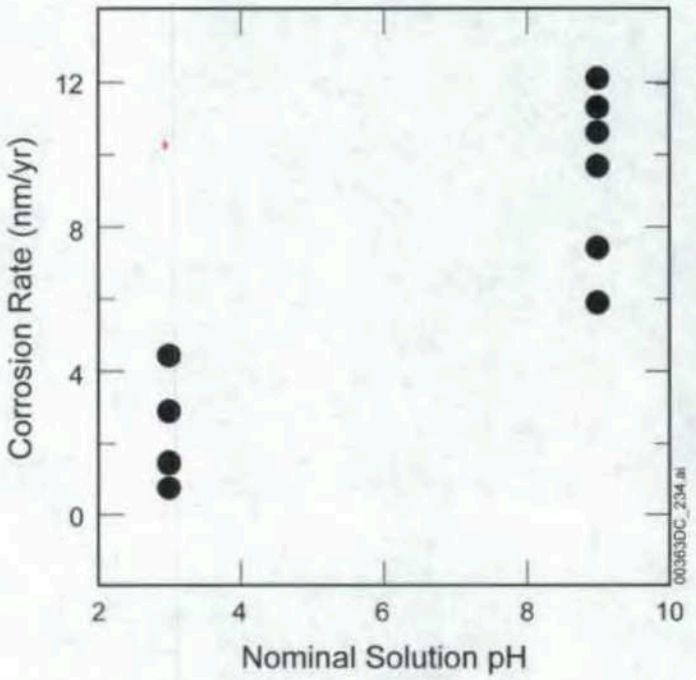

Source: BSC 2004a; DTN: MO0409MWDUGCMW.000.

Figure 26. Corrosion Rate Determined from the Weight Loss of Alloy 22 Mill Annealed and As-Welded Specimens Held in 90°C Simulated Acidified Water (pH of Approximately 3) and Simulated Concentrated Water (pH of Approximately 9 to 11) for More Than 5 Years

7. OXIDE FORMATION DUE TO THERMAL PROCESSING

This section discusses oxide scales that form at 400-750°C over years or higher temperatures (1,121°C) over minutes.

7.1 Oxide Formation on Solution-Annealed Alloy 22

In the current design plans, the waste package surface will have a surface finish created during the solution annealing step. Therefore, it is important to understand the differences between these surfaces and a polished substrate. To create the solution-annealed substrates, polished samples were placed in an oven held at 1,121°C for 20 minutes. The gas in the ovens was laboratory air. After annealing for 20 minutes, the samples were quickly cooled in a water bath of Millipore (18 Ω·cm) water and dried with compressed air. Optical inspection showed that the surfaces, which are shiny before annealing, turn a matte black after quenching due to a thick oxide scale that forms at the surface. AFM and SEM were used to image the surface morphology; TEM was used to look at the oxide in cross section; EELS was used to determine the composition in cross section.

Electrochemical Response–Potentiodynamic scans for solution-annealed samples in SAW, SCW, and BSW solutions are compared with mirror-polished samples in Figure 27. In the data shown, the current at a given voltage is lower for the solution-annealed samples in all solutions,

except above the anodic peak in SCW. Because only one trial was done for each condition, it is not known how variable these curves are, so a quantitative comparison cannot be provided. In the SCW solution, the anodic peak in the potentiodynamic curve is no longer seen, and the porous oxide film associated with the anodic peak is not found.

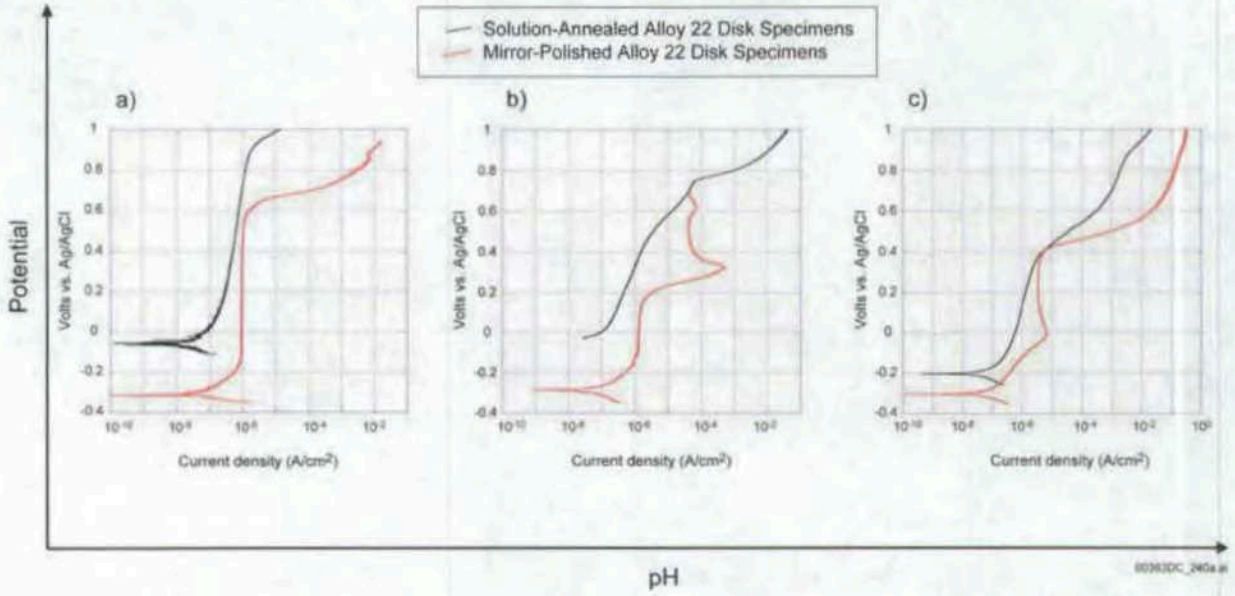

Source: DTN: LL040505512251.101.

NOTE: Potentiodynamic potential versus current density scans in (a) SAW (annealed: DEA480; polished: DEA492); (b) SCW (annealed: DEA505; polished: DEA1246); and (c) BSW (annealed: DEA481; polished: DEA461).

Figure 27. Electrochemical Response of Solution-Annealed Versus Mirror-Polished Alloy 22 Disk Specimens

Morphology–Figure 28a is an AFM image of a freshly polished surface. The underlying grain structure can be seen in this 100 μm by 100 μm scan although the height difference between neighboring grains is less than a nanometer. Figure 28b shows the same location after the solution-annealing process. The surface is covered with a polycrystalline oxide scale. Interestingly, much of the original metal grain structure can still be observed even after the thick (greater than 1 μm) oxide scale has grown. The same sample is also shown, Figure 28c, after it has been potentiostatically held in the passive region, at 250 mV in 90°C BSW for about 10 hours. No appreciable morphological changes can be observed due to the electrochemical modification.

After the solution anneal process, many of the grains have grain boundaries that are higher than the plane of the grain. These taller morphologies appear as a lighter color in the AFM images. This suggests that the polycrystalline oxide grows thicker in these regions, presumably due to greater oxygen and metal ion transport in these regions. However, this is not observed on all grain boundaries. The long boundaries typical of adjacent twinned grains shown in the lower right corner of the polished substrate (Figure 28a) do not stand out after solution annealing.

The surface morphology was also examined using a scanning electron microscope (Figure 29). At the higher magnification, Figure 29a, it can be seen that there are two distributions of crystals

with different sizes. A relatively uniform, submicrometer-sized set of crystals—as compared with the lower magnification image, Figure 29b—is concentrated at the grain boundaries, and a broader distribution of crystals with crystal sizes up to several micrometers is concentrated in the center of the grains.

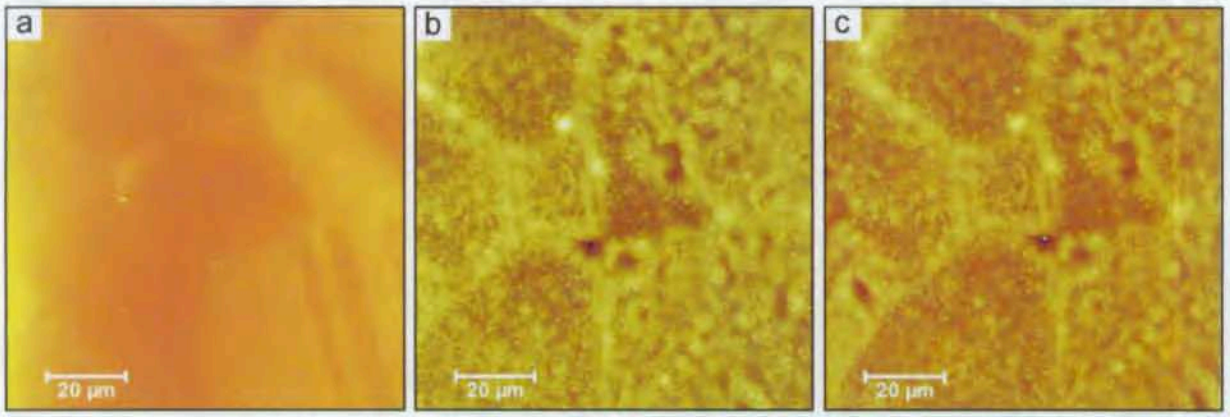

Source: DTN: LL040207612251.077.

Figure 28. AFM Images of the Surface of Sample DEA497 (a) after Polishing, (b) after the Solution Annealing Process, and (c) after Potentiostatically Holding the Sample at 250 mV in 90°C BSW Solution for about 10 Hours.

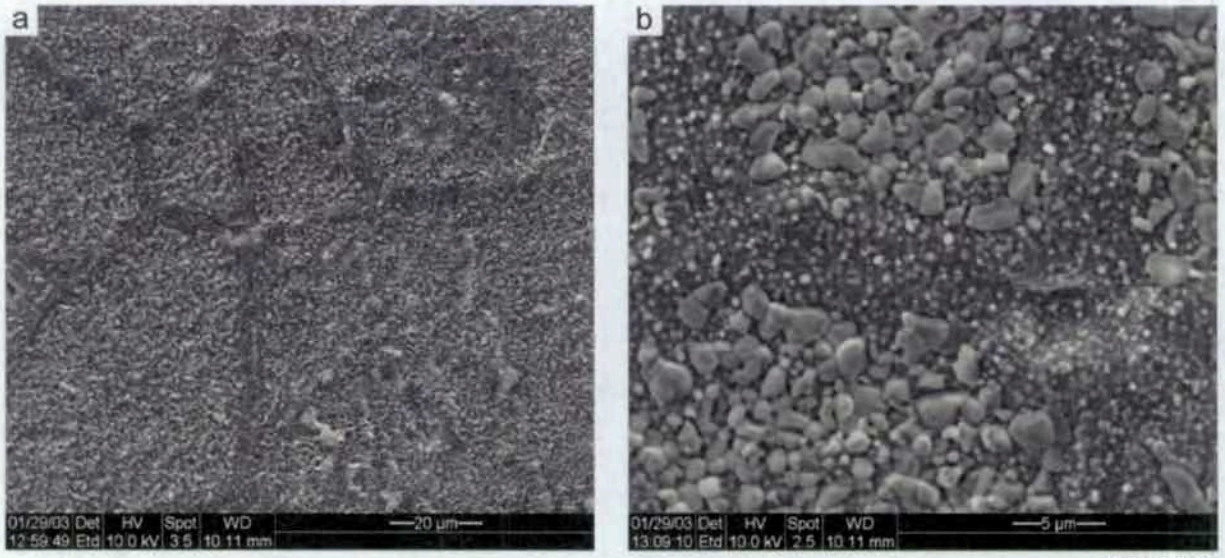

Source: DTN: LL040207412251.075.

Figure 29. SEM Images of DEA497, a Solution-Annealed Alloy 22 Substrate Shown at Two Scales

Composition of Solution-Annealed Specimens–The composition of the oxide scale was determined using cross-sectional TEM with EELS elemental mapping. Figure 30a shows a transmission electron micrograph of the cross section between the base metal, through the oxide scale and to the gold (not labeled) and platinum layers that indicate the outer edge of the oxide scale. Figure 30b shows a composite EELS image of this same region, distinguishing the nickel, iron, and chromium. By comparing with the oxygen map shown below, it is clear that the scale is an oxide where the chromium, iron, and nickel oxides have segregated. Chromium oxide (green) is closest to the base metal and has the greatest thickness (about 0.8 μm). An iron oxide forms a 0.1- to 0.5-μm layer on top of the chromium oxide, and a nickel oxide with similar thickness forms the outer layer.

The metal–oxide interface, which was flat due to polishing prior to the solution-annealing step, now appears faceted, suggesting that the metal is not consumed uniformly when it is converting to oxide. Additionally, aluminum (presumably as a minor constituent of Alloy 22) diffuses and coalesces into aluminum oxide inclusions in the metal near the metal–oxide interface. A small metallic nickel island can also be seen within the chromium oxide layer.

The oxide scale that forms on Alloy 22 during solution annealing was characterized using several methods. The approximately 1-μm thick oxide is composed of layers of chromium oxide, iron oxide, and nickel oxide. The grain boundaries have a smaller polycrystalline grain structure as compared to the center of the grains. While only a limited number of electrochemical tests were performed, the electrochemical behavior from potentiodynamic scans shows that the scale does not adversely affect the corrosion performance of solution-annealed samples. However, no long-term potentiostatic tests were performed. Oxides that form at lower temperatures (400°C to 750°C) but longer times (years) also have a thick, predominantly chromium oxide scale like the solution-annealed substrates. Based on this observation, studies on annealed samples aged at repository temperatures were not considered necessary. Microstructural evaluation of samples aged at various temperatures in the range of 427°C to 700°C showed that no significant aging will occur at repository relevant temperature (<200°C). Low-temperature aging has been shown to produce little or no evidence of precipitation or second phase particles in the grain boundaries or in the matrix and long range ordering (BSC 2004b, Section 8).

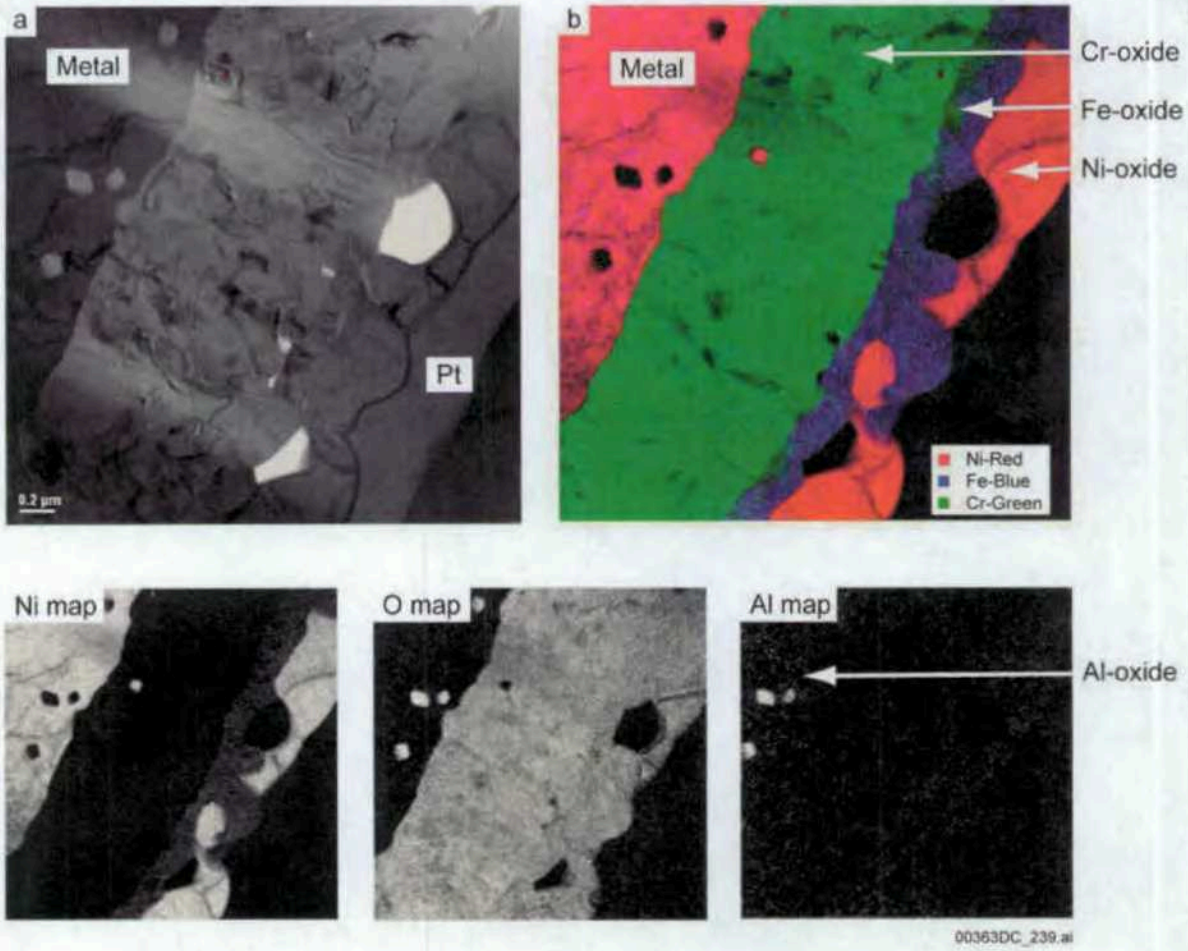

Source: DTN: LL040500512251.088.

NOTE: The TEM image (a) shows the base metal at the upper left corner and the layered structure of the chromium, iron, and nickel oxides that form during the solution annealing process. The oxide shown is greater than 1 µm thick (a 0.2-µm scale bar is shown on the image). Layers of gold (not labeled) and adjacent platinum (lower right corner) are due to the sample preparation process. The composite EELS image (b) of the same area shows nickel, iron, and chromium composition. The oxygen map (d) clearly identifies the scale as oxides. The inclusions that form in the base metal are an aluminum oxide. An inclusion of nickel metal can also be seen in the chromium-oxide layer. Molybdenum and tungsten were not detectable with EELS.

Figure 30. Cross-Sectional View of DEA498, a Solution-Annealed Alloy 22 Substrate with (a) TEM Image, (b) a composite Electron Energy-Loss Spectroscopy image of the same area, and individual maps of nickel, oxygen, and aluminum

7.2 Oxide Formation in Air at Elevated Temperature

This section summarizes the oxide formation on Alloy 22 held at temperature (25°C, 400°C, 550°C, and 750°C) for 8,000-10,000 hours (approximately one year) in dry air. In this study we show that the oxide on as-received, mill-finished Alloy 22 is an approximately 50nm thick, multi-layered structure with a chromium-rich layer nearest the metal and a nickel-rich polycrystalline oxide further from the metal. This layered oxide does not change measurably

even when aged at temperature for 10, 000 hours. However, chromium oxide crystals nucleate and grow on the oxide-air interface. This thick, chromium oxide scale layer is more pronounced at higher temperatures and is responsible for the change in coloring observed on these samples. The polycrystalline chromium oxide scale resembles the oxide formed during the "black solution anneal" process described in the previous section.

Thermal aging methods - Square rods (0.5" x 0.5" cross-section) of Alloy 22 were aged in ovens held at 400°C, 550°C, and 750°C for 8,000-10,000 hours (~1 year). The sides of the rods had two mill-finished surfaces and two, water-jet cut surfaces. The gas in the ovens was laboratory air. The thermally aged samples were compared with a control that was kept in ambient conditions since receipt. Table 5 summarizes the aging conditions.

Table 5. Aging conditions for the four samples characterized.

Sample ID	Time aged (hours)	Temperature
TS444-015P1 TS444-015P1A2	>10,000	~25°C
TS444-012F3B TS444_012F3A2	8,000	400°C
TS444-012B1B TS444-012B1A2	8,000	550°C
TS444-007G1A3	10,000	750°C

Source: Orme 2003c, p. 161 (non-Q data).

Note: Two samples (for SEM and TEM) were cut from the same bar. No TEM images were saved for the specimen held at 750°C.

Smaller samples where cut from the rod using a water-cooled saw with a diamond blade. A slow revolution rate was used to avoid heating the samples while cutting.

An optical image (Figure 31) of the samples shows that a dark scale forms on thermally aged samples and that this effect is more pronounced at higher temperatures. SEM imaging and XPS were performed to determine what this scale is and how it evolves with temperature. Cross-sectional TEM and EDS were performed to characterize the oxide at the metal interface as this layer impacts corrosion resistance.

The control (Figure 32), kept near 25°C since receipt, shows the presence of a 40-50nm thick oxide at the metal interface. The base metal near the interface has small irregular grains typical of a cold-worked, mill-finished surface. The bright line in the oxygen element map indicates that the oxide is a 40-50nm layer nearest the base-metal. The oxide has at least two layers; an amorphous (or non-diffracting) layer closest to the base metal, and a poly-crystalline, columnar region farther from the base metal (as seen by light and dark grains). The nickel map also shows variation in concentration across the oxide layer. The dark line at the metal-oxide interface indicates a nickel-poor region in the non-diffracting layer whereas the light band further from the metal indicates a nickel-rich region in the diffracting, polycrystalline layer.

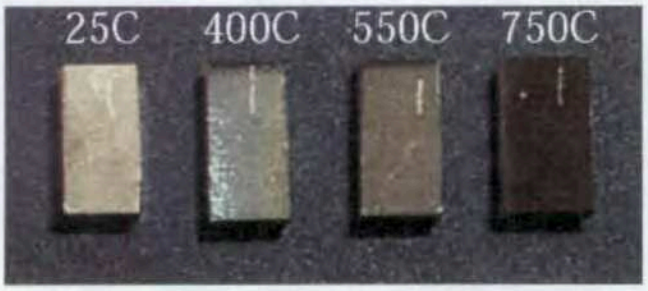

Source: Orme 2003c, p. 162 (non-Q image).

Note: The mill-finished surface is shown. The change in coloring is attributed to the growth of metal-oxides on the surface. Each sample is scratched to expose the underlying base metal. The scratched region is used to compare the elemental composition of the base metal with the overgrowth layer.

Figure 31. Optical image of the set of samples kept at ~25°C, 400°C, 550°C, and 750°C for approximately one year (see Table 5).

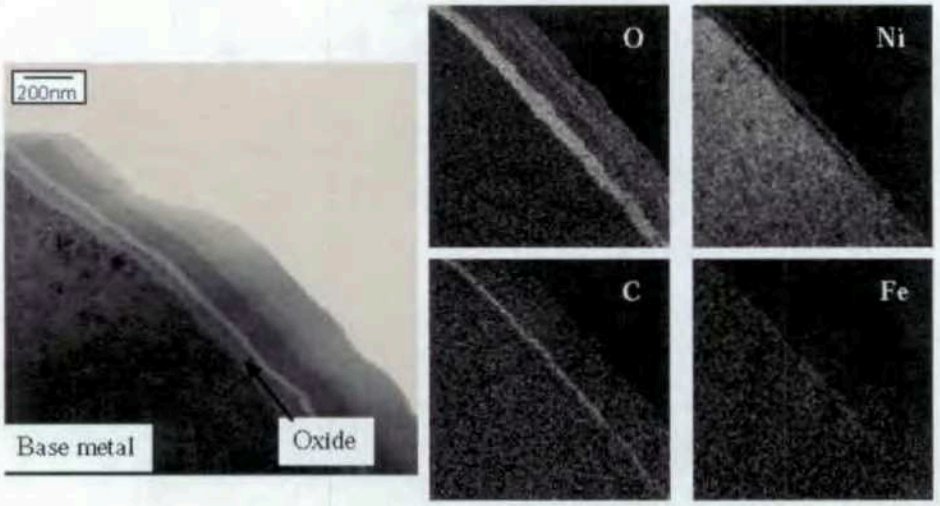

Source: Orme 2003c, p. 163 (non-Q data).

Note: The bright line in the oxygen map gives the best indication of the oxide. (The thicker banding farther from the metal is due to materials from the sample preparation). Measurements of the oxide from several images show that the oxide thickness is 40-50nm. The Nickel map shows that within the oxide layer the Nickel concentration varies with distance from the metal. This variation will be made clearer using energy dispersive spectroscopy (EDS) in Figure 34.

Figure 32. Bright field TEM image and elemental maps of a cross-section through Alloy 22 (TS444-015P1) kept under ambient conditions near 25°C.

Measurements of the oxide thickness on the sample aged at 400°C for 10,000 hours were difficult to make because the best area for TEM viewing was too thick. The best measurements of the oxide layer thickness were approximately 40-60nm thick. As seen for the control, the oxide consists of an outer polycrystalline layer with an amorphous layer closest to the metal. Energy filtered elemental maps could not be recorded on this sample due to its poor quality. However, several energy dispersive spectroscopy (EDS) line scans were performed to display the elemental information present in the oxide. No images are shown because they so closely resemble the sample aged at 550°C discussed in upcoming paragraphs.

The Alloy 22 sample aged for 8,000 hours at 550°C, also showed a very similar oxide structure. Figure 33 shows both a bright field image as well as the elemental maps of the metal-oxide interface. The oxide thickness is ~40nm. In the oxide region, both the poly-crystalline outer layer as well the non-diffracting layer seen in the previous 25°C sample is evident. In addition, there may be another very thin (<5nm) layer immediately at the metal-oxide interface. This could be a new feature resulting from the aging at temperature but we suspect that it is more evident in the 550°C sample than the 400°C and 25°C sample primarily because the image resolution is higher. The elemental maps corroborate the previous findings for both T=25°C and 400°C samples showing that the polycrystalline outer layer is a nickel oxide. As seen in the T=400°C sample, the nickel-poor inner layer is chromium-rich.

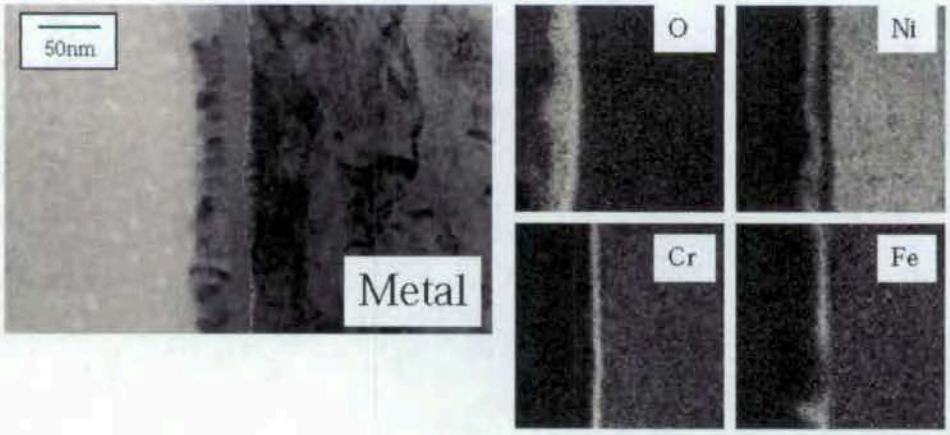

Source: Orme 2003c, p. 164 (non-Q data).

Note: The ~40nm oxide layer just to the left of the metal has several layers. The elemental maps for oxygen, nickel, chromium, and iron are shown to the right. Because the sample position drifted slightly, the elemental maps cannot be directly overlaid but instead are lined up by matching common features.

Figure 33. Bright field TEM image of Alloy 22 held at 550°C for 8,000 hours (TS444-012B1B).

A more quantitative comparison of the elemental composition across the oxide layer was made by using energy dispersive spectroscopy (EDS). A line scan was taken across the oxide as shown in Figure 34c. These plots show the same variations in concentration of the metals as previously observed, and the oxygen signal confirms that these variations are occurring within the oxide.

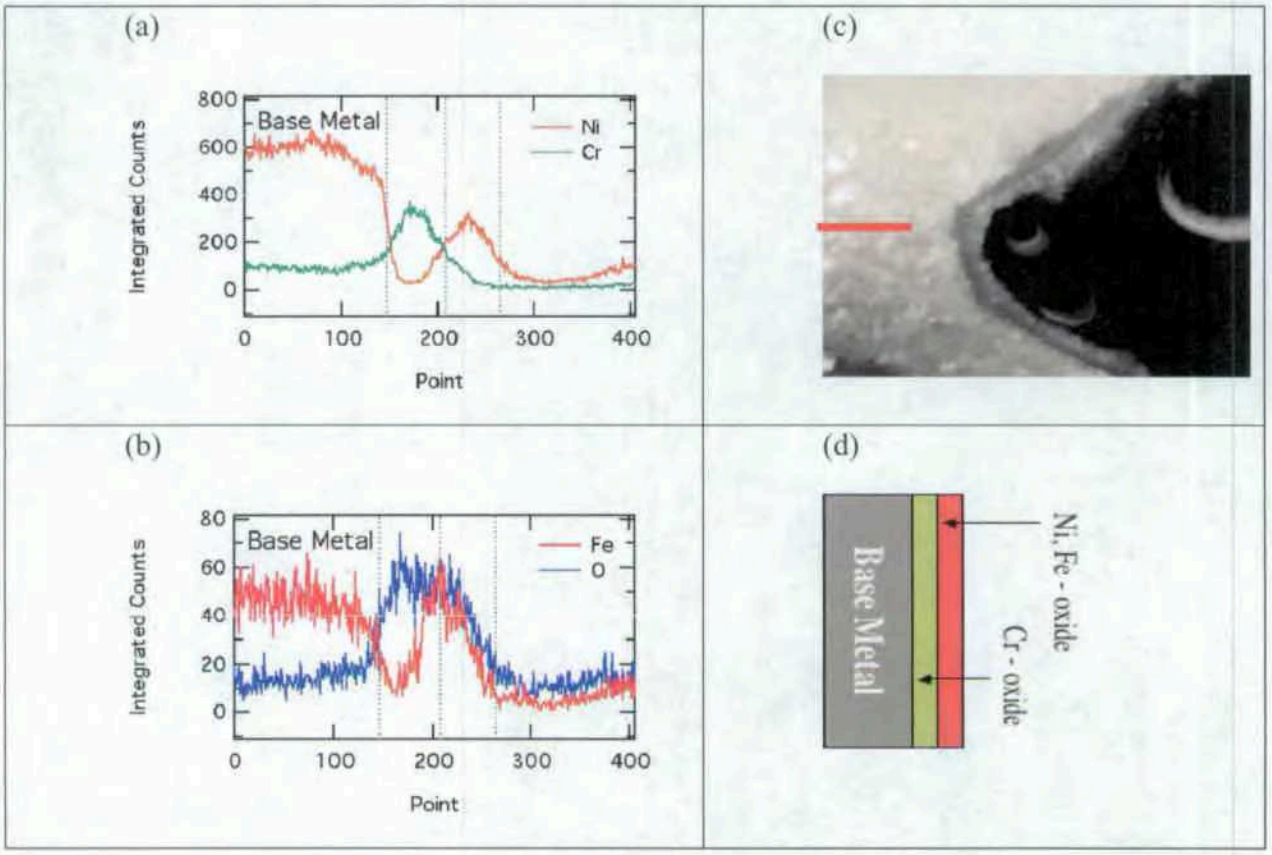

Source: Orme 2003c, p. 165 (non-Q data).

Note: The chromium and nickel spectra (a) have higher overall count rates than the iron and oxygen spectra (b) and are plotted on different vertical scales. The x-axis gives the position in arbitrary units. A line in image c) marks the approximate position where the spectra were obtained. The base metal is at the left, the oxide is at the center and empty space or glue is at the far right. Dashed grey lines mark the approximate positions of compositional transitions as determined by the half maximum values of the nickel and chromium spectra. The same locations are also marked in (b). Care was taken to isolate the O-Kα signal from the Cr-L signal. The oxygen signal is rather noisy due to the small interaction cross-section area. The spectra in (a) is consistent with a chromium-enriched and nickel-poor region closest to the base-metal, followed by a nickel-rich oxide further from the metal interface. The chromium signal indicates a higher concentration of chromium in the oxide than in the metal unlike the nickel. The iron signal more closely resembles the nickel distribution but is weaker.

Figure 34. Energy Dispersive Spectroscopy across the oxide layer showing (a) nickel and chromium (b) the weaker iron and oxygen signals, (c) the track for which the data were taken, and (d) a schematic model of the oxide.

Imaging was also attempted on the samples aged at 750°C but a region could not be found where the oxide remained intact. While the cross-sectional TEM images show little variation with temperature, it is clear from the optical images (Figure 31) that the surfaces depend upon the

aging temperature. Thus, scanning electron microscopy (SEM) was used to elucidate the differences.

The Alloy 22 surface kept under ambient conditions near 25°C shows a rough metal surface typical of a mill-finished surface (Figure 35a and 35b). The water jet cut surface was also imaged (Figure 35c and 35d) to see if the differences in processing affected the oxide growth. In Figure 35c, a particle is embedded in the surface; this is likely from slurry used to cut the metal. The surface aged at 400°C shows the formation of small crystals in some regions but these do not cover the entire surface (figure not shown). Figure 36 shows both the mill-finished and water-jet cut surfaces of the Alloy 22 sample aged at 550°C. Small crystallites cover the entire surface.

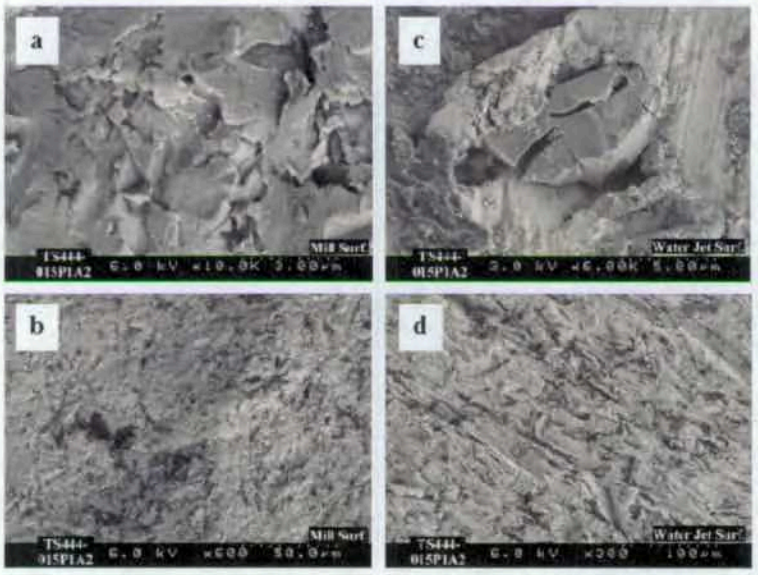

Source: Orme 2003a (p. 64), non-Q; Orme 2003c, p. 166 (non-Q data).

Note: The upper images (a) and (c) are at higher magnification than the lower images (b) and (d).

Figure 35. Scanning electron microscopy micrographs of the mill-finished (a) and (b) and water-jet cut (c) and (d) surfaces of alloy 22 aged at 25C (sample TS444-015P1A2).

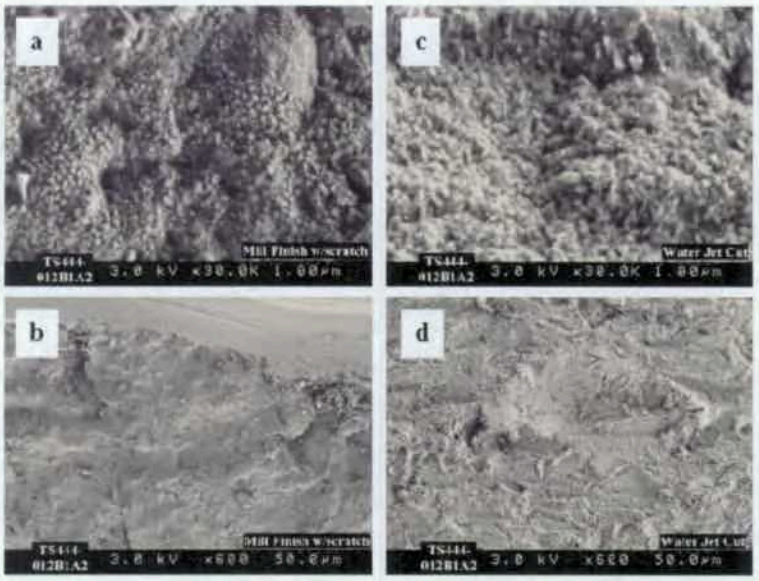

Source: Orme 2003a (p. 64), non-Q; Orme 2003c, p. 166 (non-Q data).

Note: The upper images (a) and (c) are at higher magnification than the lower images (b) and (d). Small crystallites cover the surface. The scratched region exposing the underlying metal is apparent in (b).

Figure 36. Scanning electron microscopy micrographs of the mill-finished (a) and (b) and water-jet cut (c) and (d) surfaces of Alloy 22 aged at 550°C (TS444-012B1A2).

The mill-finished surface of the sample aged at 750°C has a distribution of crystal sizes (Figure 37a). All crystals are somewhat larger in size to those formed on the sample aged at 550°C but the coverage is less uniform. In addition, larger (~1μm) well-formed crystals are distributed across the surface at a lower density. It is also evident from figure 37c that the water-jet finished surface has larger crystals that are more uniformly distributed. This is also true of the sample aged at 550°C as is seen by comparing Figures 36a and 36c.

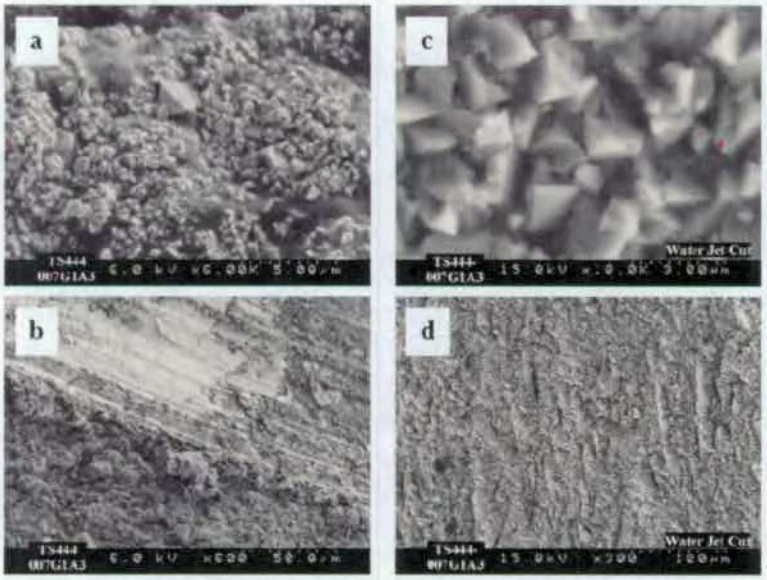

Source: Orme 2003a (p. 64, 155); Orme 2003c, p. 167 (non-Q data).

Note: The upper images (a) and (c) are at higher magnification than the lower images (b) and (d). The mill-finished surface has both small crystallites similar in size to the 550°C sample as well as larger crystals (~1μm). The scratched region exposing the underlying metal is apparent in (b).

Figure 37. Scanning electron microscopy micrographs of the mill-finished (a,b) and water-jet cut (c,d) surfaces of Alloy 22 aged at 750°C (TS444-007G1A3).

At 400°C the crystals are small and only partially cover the surface. As the temperature increases to 550°C the coverage increases. At 750°C the crystallites become larger and in some cases aggregate. One of these aggregates can be seen in Figure 38a. An EDS spectrum taken at the center of this crystal aggregate shows unambiguously that it is composed of chromium. This finding is corroborated by an occasional observation of a chromium-oxide particle in TEM cross-sections as shown in Figure 39.

X-ray photoemission spectroscopy was performed on the water-jet cut face of the Alloy 22 sample aged at 750°C (which has the most uniform coverage of crystals). The spectrum (Orme3a, p. 98, non-Q) was determined to be Cr_2O_3 by comparing with powders of Cr_2O_3 and CrO_3.

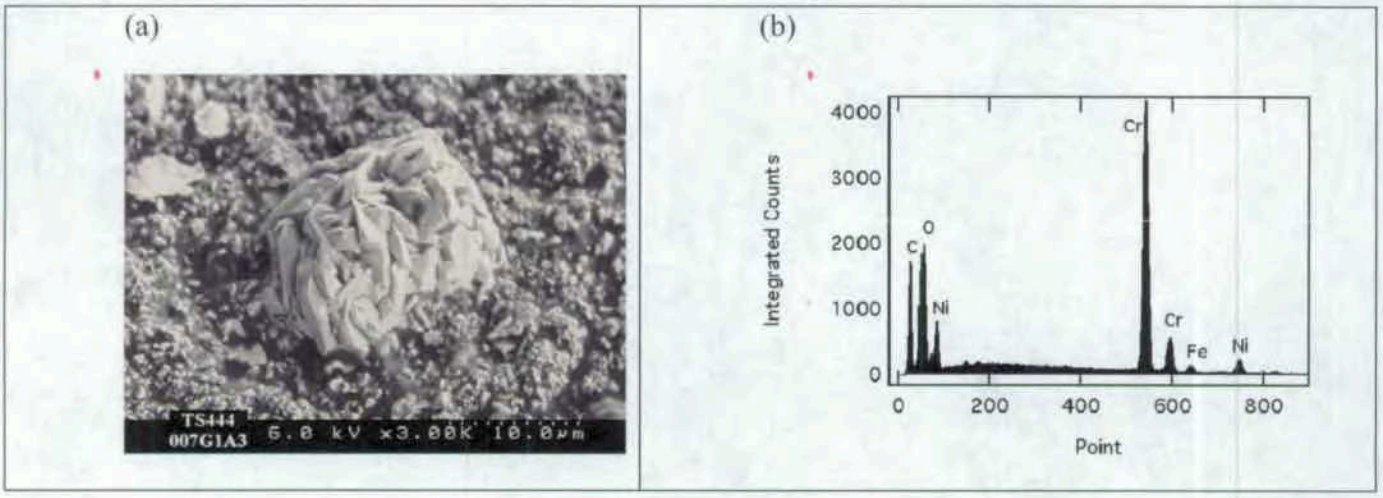

Source: Orme 2003a (p. 64, 155); Orme 2003c, p. 168 (non-Q data).

Note: Energy dispersive spectroscopy (b) focused on the crystallite in (a) demonstrated that it was rich in chromium.

Figure 38. SEM image of one of the larger crystal aggregates found on the sample aged at 750°C (TS444-007G1A3).

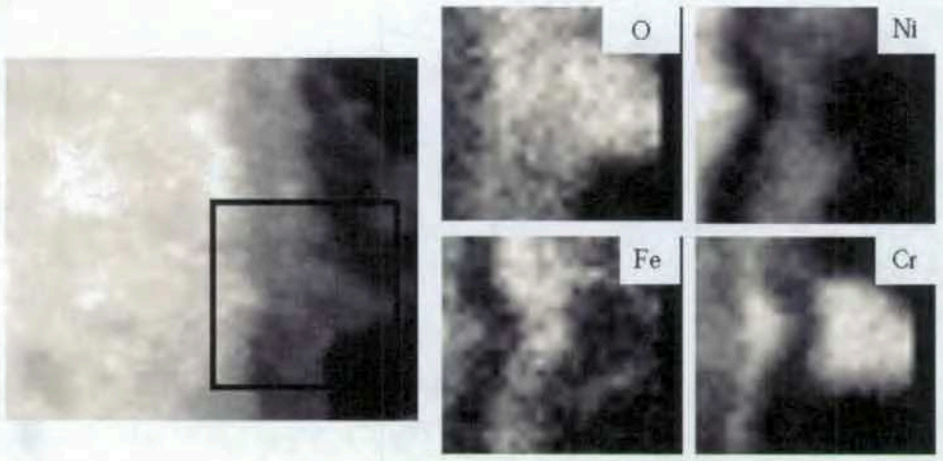

Source: Orme 2003a (p. 67); Orme 2003c, p. 168 (non-Q data).

Note: The elemental maps created using energy dispersive spectroscopy show a chromium-oxide particle at the surface of the ~40nm oxide discussed previously. The length scale is not calibrated in the scanning mode that was used to capture these maps. The approximate length is known by comparison with TEM images that were calibrated.

Figure 39. Cross-sectional TEM image of the sample (TS444-012B1B) aged at 550°C.

To summarize, the TEM data shows an oxide film whose thickness (40-60nm) and layered structure appears independent of temperature. This film is composed of an inner chromium-rich oxide that is likely amorphous and a polycrystalline Ni-oxide outer layer. At first glance this seems at odds with the optical images, which have clearly changed in color depending on temperature. And in fact, SEM images of the surfaces show Cr-rich crystallites forming on the surface with increasing density and size as a function of temperature. This suggests that the TEM sample preparation steps remove the thick Cr-rich crystals leaving behind the adherent, ~50nm thick oxide layer. This supposition is corroborated by the occasional observation in the TEM data of a Cr-oxide particles atop the ~50nm oxide. XPS data shows that the outermost polycrystalline layer is Cr_2O_3. These findings suggest that the chromium preferentially diffuses across the multi-layered oxide. Scales attributed to chromium diffusion have been noted in other nickel-based alloys (England, D.M. and A.V. Virkar, 1999, England, D.M. and A.V. Virkar, 2001) as well as in stainless steels (Cho, B., et al, 2001, Ohmi, T., et al., 1996). It has also been noted that the interface between the scale and the underlying oxide is relatively weak and can spall off during thermal cycling (Zhang, Y.F. and D.A. Shores, 1993). This is in agreement with our finding that ion milling during TEM sample preparation samples disrupts the scale layer.

TEM, SEM, and XPS were used to show that an adherent oxide layer forms during the processing stages associated with a mill finish and does not change appreciably with temperature. The major effect of temperature aging is to increase the chromium diffusion across the oxide, which results in the growth of Cr_2O_3 crystallites at the oxide-air surface.

8. SUMMARY

Oxide formation on Alloy 22 surfaces has been described for samples aged in air (25-750°C) and in solutions (90-110°C) over times ranging from days to 5 years. Oxidation of the metal forms a film on the surface that limits mass transfer between the environment and the underlying metal. Oxide composition and oxide stability have been correlated under a range of relevant repository environments, using various methodologies.

Alloy 22 develops a chromium oxide barrier layer in the range of environments tested (NaCl and multi-ionic brines at pH in the approximate range 3-12). The oxide phases expressed in the passive region are consistent (compositionally, at least) with oxides phases expected based on thermodynamic data. However, given the low metal concentrations in solution (approximately 10^{-5} mol/L), it seems more likely that the oxide layers are kinetically stable, representing a balance of oxide dissolution and metal oxidation. The measured short-term corrosion rates are low, suggesting that the dissolution kinetics of chromium oxide or oxides is very slow. The corrosion rates are also approximately constant with respect to pH in the approximate range 3-12. This implies the same for the dissolution rate of the chromium oxide material.

The formation of an oxide layer on Alloy 22 has been studied as a function of solution pH and applied potential. Oxides were tested in solutions with pH values of approximately 3 to 12. The voltages were ranged from the open circuit potential (the potential established when the metal equilibrates with its solution environment) and the breakdown potential (the potential where the metal and oxide actively dissolve). Except where noted, the samples tested were Alloy 22 base metal and Alloy 22 weld metal coupons 5/8 in. in diameter and 1/8 in. thick. The coupons were

polished to 0.02-μm finish, and held in the test solution vertically using a Teflon washer such that only the polished face was exposed to solution. All electrochemical test data was referenced to a saturated Ag/AgCl electrode (0.199 V versus standard hydrogen electrode). The oxide was found to exhibit passive behavior at all voltages tested between open circuit and breakdown potentials. Near pH 3 (±0.4), the oxide is a thin (about 4 nm thick), smooth conformal layer. At higher potentials within the passive region, the oxide becomes thinner but more compact and uniform. The oxide is predominantly chromium with some molybdenum, nickel, and tungsten. At pH near 8 (±0.5), the oxide in the passive region is similar to that found in the acidic region; it is mostly chromium oxide with lower concentrations of molybdenum and nickel. At higher voltages, the oxide transforms into a thick multilayered structure with a compact oxide (about 4 nm thick) near the surface and a porous structure between 30 and 40 nm thick at the oxide–solution interface. The outer porous oxide is predominantly nickel oxide with some iron oxide. At basic pH, the surface has a coating of porous silica scale due to dissolution from the glassware. However, silica is present in a range of relevant brines and is observed to precipitate out of solution at the oxide–solution interface. The oxide underlying the silica is compact and is composed primarily of chromium oxide. In all cases, an amorphous chromium (III) oxide is responsible for the passive behavior of the metal.

To address the question of film stability, two electrochemical metrics were used: (1) the polarization resistance and (2) the current density after holding the voltage fixed for a period of time. These were converted to a corrosion rate (or penetration rate) so they could be compared. From the polarization resistance data, it was found that the average corrosion rate was lowest in solutions near pH 8, that the welds did not differ significantly from the base metal, and that the corrosion rate did not trend with open circuit potential. The average polarization resistance corrosion rate values after 24 hours open circuit potential and their standard deviations are 2.1 ±1.2 μm/yr, 0.3 ±0.3 μm/yr, and 1.5 ±0.4 μm/yr for pH values approximately 3, 8, and 11, respectively (DTN: LL040500812251.091).

From the electrical current data, after 18 hours at fixed voltage, the primary finding was that the corrosion rate did not exhibit strong trends with either pH ranging in value from 3 to 12 or with applied voltage between the open circuit and breakdown potential. In all cases, the current decayed logarithmically to the microampere range within 18 hours. It is expected that the current would continue to decay logarithmically in time, and thus corrosion rates at times longer than 18 hours would be lower. The short-time corrosion rates allow identification of trends regarding dependence on environment (including aqueous solution composition), these rates themselves are several orders of magnitude higher than those found in long-term testing. The average final current corrosion rate values and their standard deviations are 1.9 ±3.0, 2.0 ±1.7, and 1.9 ±1.6 μm/yr for nominal pH values of 3, 8, and 11 respectively (DTN: LL040500712251.090). Because the final current did not depend strongly on potential, the final current corrosion rates were averaged over applied voltage between the open circuit and breakdown potentials. As was found in the polarization resistance measurements, the welds and base metal did not differ significantly (DTN: LL040607412251.108). Passive behavior was exhibited over a wide range of pH and applied voltage values. In all cases, chromium (III) oxide was the predominant oxide phase and this appears to be responsible for the passivity.

Equilibrium speciation modeling suggests that two chromium (III) oxide phases that may form in the passive region: Cr_2O_3 at pH 2.8 and $NiCr_2O_4$ at pH 7.5. These phases as represented in the

thermodynamic modeling are crystalline, whereas the oxide layer seen in the short-term experimental work is basically amorphous. The characterization of the experimental oxide is consistent with the amorphous equivalents, which would be less stable (more soluble) than the crystalline forms. For the oxide (whether amorphous or crystalline) and solution to be in equilibrium, sufficient metal must first dissolve into solution such that the solution becomes saturated with respect to the oxide phases. In the testing performed, the solution volume is large in comparison to the metal surface area. This, in combination with the fact that Alloy 22 has a very slow dissolution rate, means that the solution metal concentrations are approximately 10^{-5} mol/L or less (the value 10^{-5} mol/L represents an upper bound approximation assuming the integrated current only represents base metal dissolution). Therefore, the oxides seen on Alloy 22 in the short-term, large solution volume tests must be kinetically stable, and the low corrosion rates obtained are due to the slow dissolution kinetics of the chromium (III) oxide material.

It has been demonstrated that oxidation of Alloy 22 creates an amorphous Cr(III) oxide barrier that isolates the metal from its environment by limiting ionic and electronic currents. The oxide layer is compositionally consistent with the apparent equilibrium phases, Cr_2O_3 and $NiCr_2O_4$. However, the metal ion concentration in solution is below the predicted equilibrium concentration (and would be more so for the amorphous oxide). Therefore, the solution and oxide are not in equilibrium, and the measured corrosion rates must correlate with the dissolution kinetics of the Cr(III) oxide material. This suggests that a kinetically stable chromium oxide layer forms well before enough metal dissolves into solution to make the solution saturated with respect to the oxide phase. If sufficient current were to flow, or if the solution volume were small (as might be expected in vapor or water droplets on the waste package surface), then the solution would saturate, and the oxide would become thermodynamically stable (or metastable for the amorphous oxide) under fixed conditions. The dissolution rates would be expected to become even slower as the solution–oxide system moves closer to equilibrium, and thus, the corrosion rates should decrease in time. Over time, amorphous oxide must either dissolve or convert to more crystalline material.

Oxide scales that form at 400-750°C over years or higher temperatures (1,121°C) over minutes were also examined. Two scenarios were examined: solution annealing and thermal aging (in air). Solution annealing is expected to produce the actual surface of the waste package outer barrier at the time emplacement. This process was found to produce a 1-μm thick oxide layer is composed of successive sub-layers of chromium oxide (next to the metal), iron oxide, and nickel oxide. This oxide layer contains crystalline material, apparently due to the higher temperatures used in the annealing process (much higher than those expected in the repository environment). The electrochemical behavior observed in a limited number of potentiodynamic scans on annealed samples indicates that corrosion performance is not adversely affected. However, no long-term potentiostatic tests were performed. The effect of thermal aging (in air) was also considered. Alloy 22 samples were held at temperature (25°C, 400°C, 550°C, and 750°C) for 8,000-10,000 hours (approximately one year) in dry air. The oxide on as-received, mill-finished Alloy 22 is an approximately 50nm thick, multi-layered structure with a chromium-rich layer nearest the metal and a nickel-rich polycrystalline oxide further from the metal. This layered oxide does not change measurably even when aged at temperature for 10, 000 hours. However, chromium oxide crystals nucleate and grow on the oxide-air interface. This thick, chromium oxide scale layer is more pronounced at higher temperatures.

9. REFERENCES

9.1 Documents Cited

Angeliu, T.M. 2001. "Microstructural Characterization of L-Grade Stainless Steels Relative to the IGSCC Behavior in BWR Environments." *Corrosion/2001 56th Annual Conference & Exposition, March 11-16, 2001, Houston, Texas, USA.* Paper No. 01121. Houston, Texas: NACE International. TIC: 254941.

BSC (Bechtel SAIC Company) 2004a. *General Corrosion and Localized Corrosion of Waste Package Outer Barrier.* ANL-EBS-MD-000003 REV 02. Las Vegas, Nevada: Bechtel SAIC Company. ACC: DOC.20041004.0001.

BSC (Bechtel SAIC Company) 2004b. *Aging and Phase Stability of Waste Package Outer Barrier.* ANL-EBS-MD-000002 REV 02. Las Vegas, Nevada: Bechtel SAIC Company. ACC: DOC.20041005.0003.

Bulman, G.M. and Tseung, A.C.C. 1972. "The Kinetics of the Anodic Formation of the Passive Film on Stainless Steel." *Corrosion Science, 12,* 415–432. New York, New York: Pergamon Press. TIC: 255893.

Cabrera, N. and Mott, N.F. 1949. "Theory of the Oxidation of Metals." *Reports on Progress in Physics, 12,* 163–184. London, England: The Physical Society. TIC: 255982.

Cho, B., et al., *Characterization of the diffusion properties of chromium in stainless-steel oxides by photoemission spectroscopy.* Journal of Vacuum Science & Technology a-Vacuum Surfaces and Films, 2001. **19**(3): p. 998-1003. TIC: 256836.

Cragnolino, G.A.; Pan, Y-M.; Turner, D.; Pearcy, E. 2004. *Natural Analogs of High-Level Waste Container Materials - Experimental Evaluation of Josephinite.* CNWRA 2004-02. San Antonio, Texas: Center for Nuclear Waste Regulatory Analyses. TIC: 256074.

CRWMS M&O 2000. *Waste Package Degradation Process Model Report.* TDR-WIS-MD-000002 REV 00 ICN 02. Las Vegas, Nevada: CRWMS M&O. ACC: MOL.20001228.0229.

England, D.M. and A.V. Virkar, Oxidation kinetics of some nickel-based superalloy foils and electronic resistance of the oxide scale formed in air Part I. Journal of the Electrochemical Society, 1999. **146**(9): p. 3196-3202. TIC: 256838

England, D.M. and A.V. Virkar, Oxidation kinetics of some nickel-based superalloy foils in humidified hydrogen and electronic resistance of the oxide scale formed part II. Journal of the Electrochemical Society, 2001. **148**(4): p. A330-A338. TIC: 256839

Fehlner, F.P. and Mott, N.F. 1970. "Low-Temperature Oxidation." *Oxidation of Metals, 2,* (1), 59–99. New York, New York: Plenum Press. TIC: 256036.

Friend, W.Z. 1980. "Nickel-Chromium-Molybdenum Alloys." Chapter 8 of *Corrosion of Nickel and Nickel-Base Alloys.* New York, New York: Wiley-Interscience. TIC: 256002.

Haynes International. 1997. Hastelloy C-22 Alloy. Kokomo, Indiana: Haynes International. TIC: 238121.

Hodge, F.G. and Wilde, B.E. 1970. "Effect of Chloride Ion on the Anodic Dissolution Kinetics of Chromium–Nickel Binary Alloys in Dilute Sulfuric Acid." *Corrosion, 26*, (6), 146. Houston, Texas: National Association of Corrosion Engineers. TIC: 255960.

Jabs, T.; Borthen, P.; and Strehblow, H.H. 1997. "X-Ray Photoelectron Spectroscopic Examinations of Electrochemically Formed Passive Layers on Ni-Cr Alloys." *Journal of the Electrochemical Society, 144*, (4), 1231–1243. Pennington, New Jersey: Electrochemical Society. TIC: 255979.

Jones, D.A. 1996. *Principles and Prevention of Corrosion.* 2nd Edition. Upper Saddle River, New Jersey: Prentice Hall. TIC: 241233.

Kim, Y. J. "A letter report on Surface Characterization", This Letter Report Prepared under BSC Purchase Order 24540-100-PO-10508 by General Electric Global Research Center, 2/23/2004.

Lim, A.S. and Atrens, A. 1992. "ESCA Studies of Ni-Cr Alloys." *Applied Physics A: Solids and Surfaces, A54*, 343–349. Berlin, Germany: Springer-Verlag. TIC: 255984.

Lin, L.F.; Chao, C.Y.; and Macdonald, D.D. 1981. "A Point Defect Model for Anodic Passive Films. II. Chemical Breakdown and Pit Initiation." *Journal of the Electrochemical Society, 128*, (6), 1194–1198. Manchester, New Hampshire: The Electrochemical Society. TIC: 246354.

LLNL (Lawrence Livermore National Laboratory) 2003a. Acceptance Report for Scientific Investigations, for Charles Evans & Associates, Auger Electron Spectroscopy (AES) Surface Analysis Report. EAG Number: C03H3684. PO BA004609, REL 37250. ACC: MOL.20040322.0165.

LLNL 2003b. Acceptance Report for Scientific Investigations, for Charles Evans & Associates, X-Ray Photoelectron Spectroscopy (XPS)/Electron Spectroscopy For Chemical Analysis (ESCA) Surface Analysis Report. EAG Number: C03H3684. PO BA004609, REL 34672 Rev 01. ACC: MOL.20040210.0470.

Lloyd, A.C.; Shoesmith, D.W.; McIntyre, N.S.; and Noel, J.J. 2003. "Effects of Temperature and Potential on the Passive Corrosion Properties of Alloys C22 and C276." *Journal of the Electrochemical Society, 150*, (4), B120–B130. New York, New York: Electrochemical Society. TIC: 255963.

Macdonald, D.D. 1999. "Passivity—The Key to Our Metals-Based Civilization." *Pure and Applied Chemistry, 71*, (6), 951–978. Oxford, England: Blackwell Science. TIC: 249795.

MacDougall, B. 1983. "Interpretation of Log i–Log t Relationships for Nickel Passivation." *Journal of the Electrochemical Society, 130*, (1), 114–117. Manchester, New Hampshire: The Electrochemical Society. TIC: 255980.

Marcus, P. and Grimal, J.M. 1992. "The Anodic Dissolution and Passivation of Ni-Cr-Fe Alloys Studied by ESCA." *Corrosion Science, 33*, (5), 805–814. Oxford, England: Pergamon. TIC: 255959.

Marcus, P. and Maurice, V. 2000. "Passivity of Metals and Alloys." Chapter 3 of *Corrosion and Environmental Degradation.* Schütze, M., ed. Volume I. Materials Science and Technology Volume 19. New York, New York: Wiley-VCH. TIC: 249831.

Olsson, C-O.A. and Landolt, D. 2003. "Passive Films on Stainless Steels–Chemistry, Structure, and Growth." *Electrochimica Acta, 48*, 1093–1104. Oxford, England: Pergamon. TIC: 255964.

Ohmi, T., et al., *Formation of Chromium Oxide on 316l Austenitic Stainless Steel.* Journal of Vacuum Science & Technology a-Vacuum Surfaces and Films, 1996. **14**(4): p. 2505-2510. TIC:256835.

Orme, C. 2003a. Oxide Characterization. Scientific Notebook SN-LLNL-SCI-465-V1. ACC: MOL.20031024.0068.

Orme, C. 2003b. Oxide Characterization. Scientific Notebook SN-LLNL-SCI-465-V2. ACC: MOL.20031209.0148; MOL.20031110.0174.

Orme, C. 2003c. SN-LLNL-SCI-465-V1-S4, Supplement 4 to Scientific Notebook SN-LLNL-SCI-465-V1. ACC: MOL.20031024.0073.

Orme, C. 2004. Oxide Characterization. Scientific Notebook SN-LLNL-SCI-465-V3. ACC: MOL.20040520.0266.

Piron, D.L.; Koutsoukos, E.P.; and Nobe, K. 1969. "Corrosion Behavior of Nickel and Inconel in Acidic Chloride Solutions." *Corrosion, 25*, (4), 151. Houston, Texas: National Association of Corrosion Engineers. TIC: 255981.

Pourbaix, M. 1974. *Atlas of Electrochemical Equilibria in Aqueous Solutions.* Houston, Texas: National Association of Corrosion Engineers. TIC: 208955.

Qian, S., Newman, R.C., and Cottis, R.A. 1990. "Validation of a Percolation Model for Passivation of Fe-Cr Alloys: Two-Dimensional Computer Simulations." *Journal of the Electrochemical Society, 137*, (2), 435–439. Manchester, New Hampshire: The Electrochemical Society. TIC: 246354.

Schlueter, J. 2000. "U.S. Nuclear Regulatory Commission/U.S. Department of Energy Technical Exchange and Management Meeting on Container Life and Source Term (September 12-13, 2000)." Letter from J. Schlueter (NRC) to S. Brocoum (DOE/YMSCO), October 4, 2000, with enclosure. ACC: MOL.20010731.0161.

Schmuki, P.J. 2002. "From Bacon to Barriers : A Review on the Passivity of Metals and Alloys." *Journal of Solid State Electrochemistry, 6*, 145–164. Berlin, Germany: Springer-Verlag. TIC: 255958.

Schmutz, P. and Landolt, D. 1999. "In-Situ Microgravimetric Studies of Passive Alloys: Potential Sweep and Potential Step Experiments with Fe-25Cr and Fe-17Cr-33Mo in Acid and Alkaline Solution." *Corrosion Science, 41*, 2143–2163. New York, New York: Pergamon Press. TIC: 255961.

Sieradzki, K. and Newman, R.C. 1986. "A Percolation Model for Passivation in Stainless Steels" *Journal of the Electrochemical Society, 133*, (9), 1979–1980. Manchester, New Hampshire: The Electrochemical Society. TIC: 255985.

Zhang, Y.F. and D.A. Shores, *Study of Cracking and Spalling of Cr_2O_3 Scale Formed on Ni-30Cr Alloy.* Oxidation of Metals, 1993. **40**(5-6): p. 529-553. TIC:256834.

9.2 Codes, Standards, and Regulations

ASTM G 59-97. 1998. *Standard Test Method for Conducting Potentiodynamic Polarization Resistance Measurements.* West Conshohocken, Pennsylvania: American Society for Testing and Materials. TIC: 249897.

ASTM G 102-89 (Reapproved 1999) 1989. *Standard Practice for Calculation of Corrosion Rates and Related Information from Electrochemical Measurements.* West Conshohocken, Pennsylvania: American Society for Testing and Materials. TIC: 249897.

9.3 Data, Listed by Data Tracking Number

LL030300912251.036. Transmission Electron Microscopy (TEM) Images of Oxide Film on Alloy 22 during Transpassive Dissolution in Simulated Concentrated Water (SCW). Submittal date: 03/20/2003.

LL030301412251.038. Atomic Force Microscope (AFM) Images of Oxide Formation on Alloy 22 (UNS N06022). Submittal date: 05/24/2003.

LL040206412251.071. Atomic Force Microscopy Images of Various Ni-Cr-Mo Alloys Held Potentiostatically in 1 M NaCl Solutions of Various pH Values. Submittal date: 03/18/04.

LL040206512251.072. Auger Electron Spectroscopy Data from Various Ni-Cr-Mo Alloys Held Potentiostatically in 1 M NaCl Solutions of Various pH Values. Submittal date: 04/16/04.

LL040206612251.073. Electrochemical Behavior of Various Ni-Cr-Mo Based Alloys in 1 M NaCl Solutions of Various pH Values. Submittal date: 03/10/04.

LL040206712251.074. X-Ray Photoelectron Spectroscopy Data from Various Ni-Cr-Mo Alloys Held Potentiostatically in 1 M NaCl Solutions of Various pH Values. Submittal date: 04/16/04.

LL040207412251.075. Scanning Electron Microscopy Images for Various Alloy 22 Samples after Corrosion Testing. Submittal date: 03/10/04.

LL040207512251.076. Electrochemical Behavior of Alloy 22 in SAW, BSW, SCW, and 1 M NaCl Solution Buffered to pH 8. Submittal date: 03/29/04.

LL040207612251.077. Atomic Force Microscopy (AFM) Images of Various Ni-Cr-Mo Alloys Held Potentiostatically in Various Solutions. Submittal date: 03/29/04.

LL040308412251.081. Transmission Electron Microscopy (TEM) Data from Various Alloy 22 Samples after Corrosion Testing. Submittal date: 03/29/04.

LL040500512251.088. Transmission Electron Microscopy Data from Various Alloy 22 Samples after Corrosion Testing. Submittal date: 05/18/2004.

LL040500712251.090. Final Current Corrosion Rates of Alloy 22 in 1 M Sodium Chloride Held at Various pH Values. Submittal date: 05/10/2004.

LL040500812251.091. Polarization Resistance Corrosion Rates of Alloy 22 in 1 M Sodium Chloride Held at Various pH Values. Submittal date: 03/10/2004.

LL040500912251.092. Determining Oxide Thicknesses by Analysis of Cross-Sectional Transmission Electron Microscopy (TEM) Images. Submittal date: 05/24/2004.

LL040501012251.093. Alloy 22 Oxide Growth Kinetics as a Function of pH and Potentiostatic Voltage by Analysis of Log Current Density vs. Log Time Plots. Submittal date: 05/02/04.

LL040501112251.094. Depth Analysis of DEA465 Using X-Ray Photoelectron Spectroscopy. Submittal date: 05/31/2004.

LL040501212251.095. Depth Analysis of DEA495 Using X-Ray Photoelectron Spectroscopy. Submittal date: 06/08/2004.

LL040502712342.006. Equilibrium Calculations of Oxide Products from Reaction of 1 g Alloy 22 with ~1 kg of 1M NaCl at 90°C for KTI 1.08/1.09. Submittal date: 05/24/2004.

LL040505512251.101. Electrochemical Behavior of Alloy 22 in Brine Solutions of Various pH Values. KTI 1.08/1.09. Submittal date: 06/29/2004.

LL040607412251.108. Final Current Corrosion Rates of Alloy 22 Weld Specimens in Solutions with Various pH Values. KTI 1.08/1.09. Submittal date: 06/30/2004.

LL040607512251.109. Polarization Resistance Corrosion Rates of Alloy 22 Weld Specimens in Solutions with Various pH Values. KTI 1.08, 1.09. Submittal date: 07/01/2004.

MO0302SPATHDYN.000. Thermodynamic Data Input Files - Data0.ymp.R2. Submittal date: 02/05/2003.

MO0409MWDUGCMW.000. Updated General Corrosion Model Of The Waste Package Outer Barrier. Submittal date: 09/17/2004.

APPENDIX: ANALYTICAL AND TESTING DETAILS

A.1. Surface Analysis Techniques

To characterize the three-dimensional composition of the oxide, several techniques were required. Surface sensitive techniques such as X-ray Photoelectron Spectroscopy (XPS) were used to evaluate the elemental composition and oxide stoichiometry over a large (mm^2) area but from a narrow surface depth (nanometers). Cross-sectional Transmission electron microscopy provides the structure, layering, thickness, and degree of crystallinity of the oxide layer but from a limited area of the surface. Electron energy loss spectroscopy (EELS), within the TEM, provides non-quantitative elemental maps. Atomic force microscopy is used to obtain surface topographic maps with lateral range ~100μm and height resolutions of 0.1nm.

X-ray photoelectron spectroscopy (XPS) is a surface-sensitive analysis method used to determine the elemental composition and the chemical state of oxides formed on Alloy 22 coupons. Photoelectrons are generated within the X-ray penetration depth (typically many microns), but only the photoelectrons within the top three-photoelectron escape depths are detected. Escape depths are on the order of 15-35 Å, which leads to an analysis depth of ~50-100 Å. Typically, 95% of the signal originates from within this depth. All XPS measurements were performed on a PHI Quantum 2000 Quantum Scanning ESCA Microprobe using a monochromatic Al K_a source with photon energy 1486.6 electron volts (eV). The analysis area was typically 1400 μm x 300 μm. Spectra were charge corrected by aligning the Carbon C1s peak at 284.8 eV.

Cross-sectional views of the metal-oxide interface were obtained using transmission electron microscopy (TEM). Most samples were prepared using a focused ion beam "pluck out" method. Before the focused ion beam is used, a layer of gold-palladium is evaporated on to the surface to protect the oxide from beam damage during sample preparation. A much thicker platinum coating is then deposited using ion-assisted deposition. Both the Au-Pd and Pt layers can be seen in the TEM images. The Au-Pd layer, which appears dark in the bright field images shown below, can be used to mark the outer boundary of the oxide. Some samples were prepared using conventional ion milling and have an epoxy (rather than the Au-Pd layer) at the outer interface. Bright field images were obtained using a FEI-Philips TEM Model CM300FEG. Images display general oxide structure and can be used to quantify oxide thickness. Samples are typically 3μm long and images are obtained along the entire length of the sample. Images can also be correlated with elemental maps.

A.2 Electrochemical Testing

The electrochemical tests were performed in a round bottom flask placed in a hot silicone oil bath. The bath was held at a temperature such that the electrolyte solution maintained a temperature of 90°C. A volume of 900 ml of solution was placed in the flask, and connected to the flask were ports containing the follow devices: A nitrogen bubbler flowing 99.999% pure N_2 gas was used to partially deareate the solution. A condenser tube connected to a chilled water line held at 15°C prevented evaporation of the electrolyte. A Luggin probe salt bridge connected a saturated Ag/AgCl (SSC) reference electrode to the electrolyte. All potential values are referenced to the Ag/AgCl reference electrode. A platinum counter electrode consisting of a platinum wire spot-welded to a 2 x 7 cm platinum foil flag was placed in front of the specimen,

approximately 3 centimeters away from the specimen surface. The specimens were held in a vertical position to prevent corrosion products from settling on the surface, and to try to minimize the diffusion depleted region in front of the sample through convection of the electrolyte. The Luggin probe tip was placed approximately 5 mm from the surface of the specimen.

A number of electrochemical tests were performed. The solution was placed in the flask, the temperature raised to 90°C, and then the solution was de-aerated with N_2 for 1 hr. before the sample was placed into the solution. Before the sample was loaded, temperature and pH values were recorded. The sample was then inserted and the open circuit potential or corrosion potential (E_{corr}) was monitored typically for either 2 or 24 hours. All electrochemical measurements were performed using a commercial potentiostat / galvanostat / zero resistance ammeter. After the corrosion potential period one or several of the following tests were performed. Polarization resistance scans were performed according to ASTM G 102-89 on many of the samples directly after the corrosion potential monitoring. Current was recorded as the potential was stepped from 20 mV below, to 20 mV above the instantaneous E_{corr}, at a rate of 0.1667 mV/sec. The slope of this line, $\Delta V/\Delta I$, yields R_P, the polarization resistance.

Cyclic polarization scans, potentiodynamic polarization scans, or potentiostatic runs at selected potentials were performed. The cyclic polarization scans were performed to examine the passive and breakdown behavior of the alloy. The cyclic polarization scans were typically run from 200 mV below the instantaneous E_{corr} up to 5 mA or 2000 mV vs. Ag/AgCl. The voltage was then stepped back to the original E_{corr} value. A scan rate of 0.1667 mV/sec was used. The surface morphology of these samples was examined optically in order to discern any localized corrosion. Potentiodynamic scans were very similar, except the runs were stopped at either 5 mA or 2000 mV vs. Ag/AgCl, without ramping back down. Potentiostatic tests were done by stepping the potential instantaneously to a value of interest, and holding it there for 60,000 seconds.

Corrosion Rates–Corrosion rates can be determined from electrochemical measurements following guidelines outlined in ASTM G 59-97, *Standard Test Method for Conducting Potentiodynamic Polarization Resistance Measurements*. The polarization resistance can be used to calculate a corrosion current flowing at near open circuit potentials. Potentiostatic tests held at potentials in the passive region produce a corrosion current value in the passive region. Tafel extrapolation can be used to obtain a corrosion current from the potentiodynamic and cyclic polarization curve. Corrosion rates can be extrapolated from these corrosion currents by using the equivalent weight and density of the alloys examined.

Polarization Resistance–The polarization resistance *Rp* can be ultimately related to the corrosion rate *r* starting with the equation (Jones 1996, Eq. 8, p. 148):

$$R_P = \frac{B}{i_{corr}} \qquad \text{(Eq. A-1)}$$

where i_{corr} is the corrosion current density at which the cathodic and anodic reaction rates are equal, and B is related to the Tafel constants by (Jones 1996, Eq. 9, p. 148):

$$B = \frac{\beta_a \beta_c}{2.3(\beta_a + \beta_c)} \qquad \text{(Eq. A-2)}$$

where β_a is the anodic Tafel constant and β_c is the cathodic Tafel constant. From Equation A-1, i_{corr} can be calculated from Rp and B (itself obtained from the Tafel constants utilizing Equation A-2). This can then be used to obtain the corrosion rate r from the equation (cf. Jones 1996, p. 76-77):

$$r = \frac{k \cdot i_{corr} \cdot EW}{D} \qquad \text{(Eq. A-3)}$$

where k is a conversion constant, EW is the equivalent weight (in units of mol^{-1}), and D is the density of the alloy. This will yield a general corrosion rate for the alloy/electrolyte system. A conversion constant, k, with a value of 3.27 μm*g/yr*μA*mol*cm was used to yield a corrosion rate in units of μm/yr. The composition of Alloy 22 is taken from Haynes International (1997), which also gives the density of the alloy (8.69 g/cm^3). The equivalent weight was calculated to be 23.28 from a weighted average of the most common ionization states of their constituent elements (ASTM G 102). Table A-1 gives the corresponding values used for β_a and β_c. The β_a and β_c values were calculated from Tafel extrapolation (discussed below) of the cyclic polarization curves, when possible. When this was not possible, a value of 0.12 V was used.

Table A-1 Tafel Constants (β_a, β_c) used to Calculate Corrosion Rates.

Alloy	Solution	Anodic Tafel Constant (V)	Cathodic Tafel Constant (V)
Alloy 22	pH 3	0.288	0.252
Alloy 22	pH 8	0.17	0.141
Alloy 22	pH 11	0.281	0.27
Alloy 22 Weld	pH 3	0.120	0.120
Alloy 22 Weld	pH 8	0.193	0.122
Alloy 22 Weld	pH 11	0.322	0.234

Source: Non-welded, DTN: LL040500812251.091; Welded, LL040607512251.109.

Tafel Extrapolation–Tafel constants and corrosion current can be extracted from cyclic and potentiodynamic polarization curves near the open circuit potential in the activation polarization range. In this range, the activation current/potential relationship for anodic polarization (positive to the open circuit potential) is given by (Jones 1996, Eq. 10a, p. 81):

$$\eta_a = \beta_a \log \frac{i_a}{i_0} \qquad \text{(Eq. A-4)}$$

Where η_a is the anodic overpotential, β_a is the anodic Tafel constant, i_a is the anodic current density, and i_0 is the exchange current density of the anodic reaction. Similarly, the cathodic reaction can be written as (Jones 1996, Eq. 10b, p. 81):

$$\eta_c = \beta_c \log \frac{i_c}{i_0} \qquad \text{(Eq. A-5)}$$

Where η_c is the cathodic overpotential (negative), β_c is the cathodic Tafel constant, i_c is the cathodic current density, and i_0 is the exchange current density of the cathodic reaction.

The slope of the linear activation polarization portion of the potentiodynamic/cyclic polarization curves plotted as potential vs. log current density has a slope of β_a (in the anodic region) and β_c (in the cathodic region). Thus, the Tafel constants can be determined experimentally for all alloy/solution combinations. By definition, $i_a = i_c = i_{corr}$ at the open circuit potential E_{corr}. This equation, combined with the previous line fits, yields the corrosion current, i_{corr}. This can then be used in equation (A-3) to calculate a corrosion rate.

Final Corrosion Current–When a sample is held potentiostatically in the passive potential region, the current will start high, and then decrease as the passive film forms, grows, dissolves, or otherwise reaches equilibrium with its environment. This current is indicative of the corrosion rate of the alloy in the passive region. The final current from the potentiostatic scan can be used as a near-equilibrium value, and this current can be used to calculate a corrosion rate using Equation A-3.

THIS PAGE INTENTIONALLY LEFT BLANK